Mon. Not. R. Astron. Soc. **383,** 879–896 (2008) doi:10.1111/j.1365-2966.2007.12610.x

Improved constraints on dark energy from *Chandra* X-ray observations of the largest relaxed galaxy clusters

S. W. Allen,[1⋆] D. A. Rapetti,[1] R. W. Schmidt,[2] H. Ebeling,[3] R. G. Morris[1] and A. C. Fabian[4]

[1]*Kavli Institute for Particle Astrophysics and Cosmology, Stanford University, 382 Via Pueblo Mall, Stanford, CA 94305-4060, USA*
[2]*Astronomisches Rechen-Institut, Zentrum für Astronomie der Universität Heidelberg, Mönchhofstrasse 12-14, 69120 Heidelberg, Germany*
[3]*Institute for Astronomy, 2680 Woodlawn Drive, Honolulu, Hawaii 96822, USA*
[4]*Institute of Astronomy, Madingley Road, Cambridge CB3 0HA*

Accepted 2007 October 16. Received 2007 October 12; in original form 2007 May 31

ABSTRACT

We present constraints on the mean matter density, $\Omega_{\rm m}$, dark energy density, $\Omega_{\rm DE}$, and the dark energy equation of state parameter, w, using *Chandra* measurements of the X-ray gas mass fraction ($f_{\rm gas}$) in 42 hot ($kT > 5$ keV), X-ray luminous, dynamically relaxed galaxy clusters spanning the redshift range $0.05 < z < 1.1$. Using only the $f_{\rm gas}$ data for the six lowest redshift clusters at $z < 0.15$, for which dark energy has a negligible effect on the measurements, we measure $\Omega_{\rm m} = 0.28 \pm 0.06$ (68 per cent confidence limits, using standard priors on the Hubble constant, H_0, and mean baryon density, $\Omega_{\rm b}\,h^2$). Analysing the data for all 42 clusters, employing only weak priors on H_0 and $\Omega_{\rm b}\,h^2$, we obtain a similar result on $\Omega_{\rm m}$ and a detection of the effects of dark energy on the distances to the clusters at ∼99.99 per cent confidence, with $\Omega_{\rm DE} = 0.86 \pm 0.21$ for a non-flat ΛCDM model. The detection of dark energy is comparable in significance to recent type Ia supernovae (SNIa) studies and represents strong, independent evidence for cosmic acceleration. Systematic scatter remains undetected in the $f_{\rm gas}$ data, despite a weighted mean statistical scatter in the distance measurements of only ∼5 per cent. For a flat cosmology with a constant dark energy equation of state, we measure $\Omega_{\rm m} = 0.28 \pm 0.06$ and $w = -1.14 \pm 0.31$. Combining the $f_{\rm gas}$ data with independent constraints from cosmic microwave background and SNIa studies removes the need for priors on $\Omega_{\rm b}\,h^2$ and H_0 and leads to tighter constraints: $\Omega_{\rm m} = 0.253 \pm 0.021$ and $w = -0.98 \pm 0.07$ for the same constant-w model. Our most general analysis allows the equation of state to evolve with redshift. Marginalizing over possible transition redshifts $0.05 < z_{\rm t} < 1$, the combined $f_{\rm gas}$ + CMB + SNIa data set constrains the dark energy equation of state at late and early times to be $w_0 = -1.05 \pm 0.29$ and $w_{\rm et} = -0.83 \pm 0.46$, respectively, in agreement with the cosmological constant paradigm. Relaxing the assumption of flatness weakens the constraints on the equation of state by only a factor of ∼2. Our analysis includes conservative allowances for systematic uncertainties associated with instrument calibration, cluster physics and data modelling. The measured small systematic scatter, tight constraint on $\Omega_{\rm m}$ and powerful constraints on dark energy from the $f_{\rm gas}$ data bode well for future dark energy studies using the next generation of powerful X-ray observatories, such as Constellation-X.

Key words: cosmic microwave background – cosmological parameters – cosmology: observations – dark matter – distance scale – X-rays: galaxies: clusters.

1 INTRODUCTION

The matter content of the largest clusters of galaxies is expected to provide an almost fair sample of the matter content of the Universe (e.g. White et al. 1993; Eke, Navarro & Frenk 1998; Frenk et al. 1999). The ratio of baryonic-to-total mass in clusters should, therefore, closely match the ratio of the cosmological parameters $\Omega_{\rm b}/\Omega_{\rm m}$. The baryonic mass content of clusters is dominated by the X-ray emitting gas, the mass of which exceeds the mass of optically luminous material by a factor of ∼6, with other sources of baryonic matter being negligible (Fukugita, Hogan & Peebles 1998; Lin &

⋆E-mail: swa@stanford.edu

Mohr 2004). The combination of robust measurements of the baryonic mass fraction in clusters from X-ray observations together with a determination of Ω_b from cosmic microwave background (CMB) data or big bang nucleosynthesis calculations and a constraint on the Hubble constant, can therefore be used to measure Ω_m (e.g. Fabian 1991; White & Frenk 1991; Briel, Henry & Böhringer 1992; White et al. 1993; David, Jones & Forman 1995; White & Fabian 1995; Evrard 1997; Ettori & Fabian 1999; Mohr, Mathiesen & Evrard 1999; Roussel, Sadat & Blanchard 2000; Grego et al. 2001; Allen, Schmidt & Fabian 2002a; Allen et al. 2003; Ettori, Tozzi & Rosati 2003; Lin, Mohr & Stanford 2003; Sanderson & Ponman 2003; Allen et al. 2004; LaRoque et al. 2006). This method currently provides one of our best constraints on Ω_m and is remarkably simple and robust in terms of its underlying assumptions.

Measurements of the apparent evolution of the cluster X-ray gas mass fraction, hereafter f_{gas}, can also be used to probe the acceleration of the Universe (Allen et al. 2004; see also Sasaki 1996; Pen 1997; Allen et al. 2002a, 2003; Ettori et al. 2003; LaRoque et al. 2006). This constraint originates from the dependence of the f_{gas} measurements, which derive from the observed X-ray gas temperature and density profiles, on the assumed distances to the clusters, $f_{gas} \propto d^{1.5}$.[1] The expectation from non-radiative hydrodynamical simulations is that for the largest ($kT \gtrsim 5$ keV), dynamically relaxed clusters and for measurement radii beyond the innermost core ($r \gtrsim r_{2500}$), f_{gas} should be approximately constant with redshift (Eke et al. 1998; Crain et al. 2007). However, possible systematic variation of f_{gas} with redshift can be accounted for in a straightforward manner, so long as the allowed range of such variation is constrained by numerical simulations or other, complementary data (Eke et al. 1998; Bialek, Evrard & Mohr 2001; Muanwong et al. 2002; Borgani et al. 2004; Ettori et al. 2004; Kay et al. 2004; Kravtsov, Nagai & Vikhlinin 2005; Ettori et al. 2006; Nagai, Vikhlinin & Kravtsov 2007a).

The first clear detection of cosmic acceleration using the f_{gas} technique was made by Allen et al. (2004) using *Chandra* observations of 26 hot ($kT \gtrsim 5$ keV), X-ray luminous ($L_{bol} \gtrsim 10^{45}\, h_{70}^{-2}$ erg s^{-1}), dynamically relaxed clusters spanning the redshift range 0.07–0.9. The total *Chandra* exposure used in that work, after all screening procedures were applied, was ∼830 ks. That study led to a $\sim 3\sigma$ detection of the acceleration of the Universe and a tight constraint on the mean mass density $\Omega_m = 0.25 \pm 0.04$ (see also Allen et al. 2002a, 2003; Ettori et al. 2003; LaRoque et al. 2006) in excellent agreement with independent findings from CMB studies (e.g. Spergel et al. 2003, 2007), type Ia supernovae (SNIa) data (e.g. Riess et al. 2004; Astier et al. 2006), galaxy redshift surveys (e.g. Cole et al. 2005; Eisenstein et al. 2005; Percival et al. 2007) and X-ray cluster number counts (e.g. Mantz et al. 2007).

Here we present a significant extension of the Allen et al. (2004) work. Our expanded sample contains 42 clusters spanning the redshift range $0.05 < z < 1.1$. We incorporate new, deeper exposures for some of the original clusters, as well as new targets, approximately doubling the total exposure time used. Our analysis method incorporates conservative allowances for systematic uncertainties associated with instrument calibration, cluster physics and data modelling. As before, we employ rigorous selection criteria, restricting the analysis to the hottest, most dynamically relaxed clusters. We show that this leads to remarkably small intrinsic scatter in the f_{gas} measurements, with no apparent systematic dependence of f_{gas} on temperature for clusters with $kT > 5$ keV. Our method imposes a minimum of prior constraints and does not require that the density and temperature profiles of the X-ray emitting gas follow simple parametrized forms. We make our f_{gas} measurements for each cluster at the radius r_{2500} in the reference Lambda cold dark matter (ΛCDM) cosmology, corresponding to an angle $\theta_{2500}^{\Lambda CDM}$, for which the mean enclosed mass density is 2500 times the critical density of the Universe at the redshift of the cluster. This corresponds to about one quarter of the virial radius[2] and represents a near-optimal choice for *Chandra* studies, being sufficiently large to provide small systematic scatter but not so large as to be hampered by systematic uncertainties in the background modelling. We compare our f_{gas} measurements to results from other, independent studies and to the predictions from current hydrodynamical simulations.

Our analysis of cosmological parameters employs a Markov Chain Monte Carlo (MCMC) approach, which is efficient and allows for the simple inclusion of priors and a comprehensive study of the effects of systematic uncertainties. We present results based on studies of the f_{gas} data alone (adopting simple priors on $\Omega_b h^2$ and h) and for the f_{gas} data used in combination with current CMB constraints (in which case the priors on $\Omega_b h^2$ and h can be dropped) and SNIa data (Astier et al. 2006; Jha, Riess & Kirshner 2007; Riess et al. 2007; Wood-Vasey et al. 2007). We highlight the power of the data combinations for cosmological work, particularly in constraining the mean matter and dark energy densities of the Universe and the dark energy equation of state.

The f_{gas} measurements are quoted for a flat ΛCDM reference cosmology with $h = H_0/100\,\mathrm{km\,s^{-1}\,Mpc^{-1}} = 0.7$ and $\Omega_m = 0.3$.

2 X-RAY OBSERVATIONS AND ANALYSIS

2.1 Sample selection

Our sample consists of 42 hot, X-ray luminous, dynamically relaxed galaxy clusters spanning the redshift range $0.05 < z < 1.1$. The systems have mass-weighted X-ray temperatures measured within r_{2500}, $kT_{2500} \gtrsim 5$ keV and exhibit a high degree of dynamical relaxation in their *Chandra* images (Million et al., in preparation), with sharp central X-ray surface brightness peaks, short central cooling times ($t_{cool} \leqslant$ a few $\times 10^9$ yr) minimal isophote centroid variations (e.g. Mohr et al. 1995) and low X-ray power ratios (Buote & Tsai 1995, 1996; Jeltema et al. 2005). Although target selection is

[1] To understand the origin of the $f_{gas} \propto d^{1.5}$ dependence, consider a spherical region of observed angular radius θ within which the mean gas mass fraction is measured. The physical size, R, is related to the angle θ as $R = \theta d_A$. The X-ray luminosity emitted from within this region, L_X, is related to the detected flux, F_X, as $L_X = 4\pi d_L^2 F_X$, where d_L is the luminosity distance and $d_A = d_L/(1+z)^2$ is the angular diameter distance. Since the X-ray emission is primarily due to collisional processes (bremsstrahlung and line emission) and is optically thin, we may also write $L_X \propto n^2 V$, where n is the mean number density of colliding gas particles and V is the volume of the emitting region, with $V = 4\pi(\theta d_A)^3/3$. Considering the cosmological distance dependences, we see that $n \propto d_L/d_A^{1.5}$, and that the observed gas mass within the measurement radius $M_{gas} \propto nV \propto d_L d_A^{1.5}$. The total mass, M_{tot}, determined from the X-ray data under the assumption of hydrostatic equilibrium, $M_{tot} \propto d_A$. Thus, the X-ray gas mass fraction measured within angle θ is $f_{gas} = M_{gas}/M_{tot} \propto d_L d_A^{0.5}$.

[2] The virial radius is defined as the radius within which the density contrast $\Delta_c = 178\ \Omega_m(z)^{0.45}$, with respect to the critical density (Lahav et al. 1991; Eke et al. 1998).

based only on these morphological X-ray characteristics, the clusters also exhibit other signatures of dynamical relaxation including minimal evidence for departures from hydrostatic equilibrium in X-ray pressure maps (Million et al., in preparation). The notable exceptions are Abell 2390, RXJ1347.5−1145, MACS1427.3+4408 and MACSJ0744.9+3927, for which clear substructure is observed between position angles of 255°–15°, 90°–190°, 160°–280° and 210°–330°, respectively (Allen, Schmidt & Fabian 2002b; Morris et al., in preparation; Million et al., in preparation). The regions associated with obvious substructure in these clusters have been excluded from the analysis. The bulk of the clusters at $z > 0.3$ were identified in the MACS survey (Ebeling, Edge & Henry 2001; Ebeling et al. 2007). Of the 70 MACS clusters with sufficient data on the *Chandra* archive at the time of observation to enable detailed spatially resolved spectroscopy, 22/70 are identified as being sufficiently relaxed to be included in the present study.

The restriction to clusters with the highest possible degree of dynamical relaxation, for which the assumption of hydrostatic equilibrium should be most valid, minimizes systematic scatter in the $f_{\rm gas}$ data (Section 5.3) and allows for the most precise and robust determination of cosmological parameters. The restriction to the hottest ($kT > 5$ keV), relaxed systems further simplifies the analysis: for galaxies, groups and clusters with $kT \lesssim 4$ keV, the baryonic mass fraction is both expected and observed to rise systematically with increasing temperature, with the systematic scatter being largest in the coolest systems (e.g. Bialek et al. 2001; Muanwong et al. 2002; Ettori et al. 2004; Kravtsov et al. 2005; Vikhlinin et al. 2006). As shown in Sections 3.1 and 5.3, for the hot, relaxed clusters studied here, $f_{\rm gas}$ exhibits no dependence on temperature and the intrinsic scatter is small.

2.2 Data reduction

The *Chandra* observations were carried out using the Advanced CCD Imaging Spectrometer (ACIS) between 1999 August 30 and 2005 June 28. The standard level-1 event lists produced by the *Chandra* pipeline processing were reprocessed using the CIAO (version 3.2.2) software package, including the appropriate gain maps and calibration products. Bad pixels were removed and standard grade selections applied. Where possible, the extra information available in VFAINT mode was used to improve the rejection of cosmic ray events. The data were cleaned to remove periods of anomalously high background using the standard energy ranges and time bins recommended by the *Chandra* X-ray Centre. The net exposure times after cleaning are summarized in Table 1. The total good exposure is 1.63 Ms, approximately twice that of the Allen et al. (2004) study.

2.3 Spectral analysis

The spectral analysis was carried out using an updated version of the techniques described by Allen et al. (2004) and Schmidt & Allen (2007). In brief, concentric annular spectra were extracted from the cleaned event lists, centred on the coordinates listed in Table 1. Emission associated with X-ray point sources or obvious substructure (Table 2) was excluded. The spectra were analysed using XSPEC (version 11.3; Arnaud 1996), the MEKAL plasma emission code (Kaastra & Mewe 1993; incorporating the Fe-L calculations of Liedhal, Osterheld & Goldstein 1995) and the photoelectric absorption models of Balucinska-Church & McCammon (1992). The emission from each spherical shell was modelled as a single-phase plasma. The abundances of the elements in each shell were assumed to vary with a common ratio, Z, with respect to solar values. The absorbing column densities were fixed to the Galactic values determined from H I studies (Dickey & Lockman 1990), with the exception of Abell 478 and PKS0745−191 where the value was allowed to fit freely. (For Abell 478, the absorbing column density was allowed to vary as a function of radius, as was shown to be required by Allen et al. 1993). We have included standard correction factors to account for time-dependent contamination along the instrument light path. In addition, we have incorporated a small correction to the high-resolution mirror assembly model in CIAO 3.2.2, which takes the form of an 'inverse' edge with an energy, $E = 2.08$ keV and optical depth $\tau = -0.1$ (H. Marshall, private communication) and also boosted the overall effective area by 6 per cent, to better match later calibration data (A. Vikhlinin, private communication). These corrections lead to an excellent match with results based on later calibration data, available in CIAO 3.4. Only data in the 0.8–7.0 keV energy range were used in the analysis (with the exceptions of the earliest observations of 3C 295, Abell 1835 and Abell 2029, where a wider 0.6–7.0 keV band was used to enable better modelling of the soft X-ray background).

For the nearer clusters ($z < 0.3$), background spectra were extracted from the blank-field data sets available from the *Chandra* X-ray centre. These were cleaned in an identical manner to the target observations. In each case, the normalizations of the background files were scaled to match the count rates in the target observations measured in the 9.5–12 keV band. Where required, e.g. due to the presence of strong excess soft emission in the field, a spectral model for additional soft background emission was included in the analysis. For the more distant systems (as well as for the first observation of Abell 1835, the ACIS-I observation of Abell 383, and the observations of Abell 2537, RXJ 2129.6+0005 and Zwicky 3146) background spectra were extracted from appropriate, source free regions of the target data sets. (We have confirmed that similar results are obtained using the blank-field background data sets.) In order to minimize systematic errors, we have restricted our spectral analysis to radii within which systematic uncertainties in the background subtraction (established by the comparison of different background subtraction methods) are smaller than the statistical uncertainties in the results. All results are drawn from ACIS chips 0, 1, 2, 3 and 7 which have the most accurate calibration, although ACIS chip 5 was also used to study the soft X-ray background in ACIS-S observations.

Separate photon-weighted response matrices and effective area files were constructed for each region using calibration files appropriate for the period of observations. The spectra for all annuli for a given cluster were modelled simultaneously in order to determine the deprojected X-ray gas temperature and metallicity profiles, under the assumption of spherical symmetry. The extended C-statistic, available in XSPEC, was used for all spectral fitting.

2.4 Measuring the mass profiles

The details of the mass analysis and results on the total mass and dark matter profiles are presented by Schmidt & Allen (2007). In brief, X-ray surface brightness profiles in the 0.8–7.0 keV band were extracted from background subtracted, flat-fielded *Chandra* images with 0.984×0.984 arcsec^2 pixel. The profiles were centred on the coordinates listed in Table 1. Under the assumptions of hydrostatic equilibrium and spherical symmetry, the observed X-ray surface brightness profiles and deprojected X-ray gas temperature profiles

Table 1. Summary of the *Chandra* observations. Columns list the target name, observation date, detector used, observation mode, net exposure after all cleaning and screening processes were applied and right ascension (RA) and declination (Dec.) for the X-ray centres. Where multiple observations of a single cluster have been used, these are listed separately.

Name	Date	Detector	Mode	Exposure (ks)	RA (J2000)	Dec. (J2000)
Abell 1795(1)	2002 June 10	ACIS-S	VFAINT	13.2	13 48 52.4	26 35 38
Abell 1795(2)	2004 January 14	ACIS-S	VFAINT	14.3	13 48 52.4	26 35 38
Abell 1795(3)	2004 January 18	ACIS-I	VFAINT	9.6	13 48 52.4	26 35 38
Abell 2029(1)	2000 April 12	ACIS-S	FAINT	19.2	15 10 56.2	05 44 41
Abell 2029(2)	2004 January 08	ACIS-S	FAINT	74.8	15 10 56.2	05 44 41
Abell 2029(3)	2004 December 17	ACIS-I	VFAINT	9.4	15 10 56.2	05 44 41
Abell 478(1)	2001 January 27	ACIS-S	FAINT	39.9	04 13 25.2	10 27 55
Abell 478(2)	2004 September 13	ACIS-I	VFAINT	7.4	04 13 25.2	10 27 55
PKS0745−191(1)	2001 June 16	ACIS-S	VFAINT	17.4	07 47 31.7	−19 17 45
PKS0745−191(2)	2004 September 24	ACIS-I	VFAINT	9.2	07 47 31.7	−19 17 45
Abell 1413	2001 May 16	ACIS-I	VFAINT	64.5	11 55 18.1	23 24 17
Abell 2204(1)	2000 July 29	ACIS-S	FAINT	10.1	16 32 47.2	05 34 32
Abell 2204(2)	2004 September 20	ACIS-I	VFAINT	8.5	16 32 47.2	05 34 32
Abell 383(1)	2000 November 16	ACIS-S	FAINT	18.0	02 48 03.5	−03 31 45
Abell 383(2)	2000 November 16	ACIS-I	VFAINT	17.2	02 48 03.5	−03 31 45
Abell 963	2000 October 11	ACIS-S	FAINT	35.8	10 17 03.8	39 02 49
RXJ0439.0+0520	2000 August 29	ACIS-I	VFAINT	7.6	04 39 02.3	05 20 44
RXJ1504.1−0248	2005 March 20	ACIS-I	VFAINT	29.4	15 04 07.9	−02 48 16
Abell 2390	2003 September 11	ACIS-S	VFAINT	79.2	21 53 36.8	17 41 44
RXJ2129.6+0005	2000 October 21	ACIS-I	VFAINT	7.6	21 29 39.9	00 05 20
Abell 1835(1)	1999 December 11	ACIS-S	FAINT	18.0	14 01 01.9	02 52 43
Abell 1835(2)	2000 April 29	ACIS-S	FAINT	10.3	14 01 01.9	02 52 43
Abell 611	2001 November 03	ACIS-S	VFAINT	34.5	08 00 56.8	36 03 24
Zwicky 3146	2000 May 10	ACIS-I	FAINT	41.4	10 23 39.4	04 11 14
Abell 2537	2004 September 09	ACIS-S	VFAINT	36.0	23 08 22.1	−02 11 29
MS2137.3−2353(1)	1999 November 18	ACIS-S	VFAINT	20.5	21 40 15.2	−23 39 40
MS2137.3−2353(2)	2003 November 18	ACIS-S	VFAINT	26.6	21 40 15.2	−23 39 40
MACSJ0242.6−2132	2002 February 07	ACIS-I	VFAINT	10.2	02 42 35.9	−21 32 26
MACSJ1427.6−2521	2002 June 29	ACIS-I	VFAINT	14.7	14 27 39.4	−25 21 02
MACSJ2229.8−2756	2002 November 13	ACIS-I	VFAINT	11.8	22 29 45.3	−27 55 37
MACSJ0947.2+7623	2000 October 20	ACIS-I	VFAINT	9.6	09 47 13.1	76 23 14
MACSJ1931.8−2635	2002 October 20	ACIS-I	VFAINT	12.2	19 31 49.6	−26 34 34
MACSJ1115.8+0129	2003 January 23	ACIS-I	VFAINT	10.2	11 15 52.1	01 29 53
MACSJ1532.9+3021(1)	2001 August 26	ACIS-S	VFAINT	9.4	15 32 53.9	30 20 59
MACSJ1532.9+3021(2)	2001 September 06	ACIS-I	VFAINT	9.2	15 32 53.9	30 20 59
MACSJ0011.7−1523(1)	2002 November 20	ACIS-I	VFAINT	18.2	00 11 42.9	−15 23 22
MACSJ0011.7−1523(2)	2005 June 28	ACIS-I	VFAINT	32.1	00 11 42.9	−15 23 22
MACSJ1720.3+3536(1)	2002 November 03	ACIS-I	VFAINT	16.6	17 20 16.8	35 36 27
MACSJ1720.3+3536(2)	2005 November 22	ACIS-I	VFAINT	24.8	17 20 16.8	35 36 27
MACSJ0429.6−0253	2002 February 07	ACIS-I	VFAINT	19.1	04 29 36.1	−02 53 08
MACSJ0159.8−0849(1)	2002 October 02	ACIS-I	VFAINT	14.1	01 59 49.4	−08 49 58
MACSJ0159.8−0849(2)	2004 December 04	ACIS-I	VFAINT	28.9	01 59 49.4	−08 49 58
MACSJ2046.0−3430	2005 June 28	ACIS-I	VFAINT	8.9	20 46 00.5	−34 30 17
MACSJ1359.2−1929	2005 March 17	ACIS-I	VFAINT	9.2	13 59 10.3	−19 29 24
MACSJ0329.7−0212(1)	2002 December 24	ACIS-I	VFAINT	16.8	03 29 41.7	−02 11 48
MACSJ0329.7−0212(2)	2004 December 06	ACIS-I	VFAINT	31.1	03 29 41.7	−02 11 48
RXJ1347.5−1145(1)	2000 March 03	ACIS-S	VFAINT	8.6	13 47 30.6	−11 45 10
RXJ1347.5−1145(2)	2000 April 29	ACIS-S	FAINT	10.0	13 47 30.6	−11 45 10
RXJ1347.5−1145(3)	2003 September 03	ACIS-I	VFAINT	49.3	13 47 30.6	−11 45 10
3C295(1)	1999 August 30	ACIS-S	FAINT	15.4	14 11 20.5	52 12 10
3C295(2)	2001 May 18	ACIS-I	FAINT	72.4	14 11 20.5	52 12 10
MACSJ1621.6+3810(1)	2002 October 18	ACIS-I	VFAINT	7.9	16 21 24.8	38 10 09
MACSJ1621.6+3810(2)	2004 December 11	ACIS-I	VFAINT	32.2	16 21 24.8	38 10 09
MACSJ1621.6+3810(3)	2004 December 25	ACIS-I	VFAINT	26.1	16 21 24.8	38 10 09
MACS1427.3+4408	2005 February 12	ACIS-I	VFAINT	8.70	14 27 16.2	44 07 31
MACSJ1311.0−0311	2005 April 20	ACIS-I	VFAINT	56.2	13 11 01.6	−03 10 40
MACSJ1423.8+2404	2003 August 18	ACIS-S	VFAINT	113.5	14 23 47.9	24 04 43
MACSJ0744.9+3927(1)	2001 November 12	ACIS-I	VFAINT	17.1	07 44 52.9	39 27 27
MACSJ0744.9+3927(2)	2003 January 04	ACIS-I	VFAINT	15.6	07 44 52.9	39 27 27
MACSJ0744.9+3927(3)	2004 December 03	ACIS-I	VFAINT	41.3	07 44 52.9	39 27 27

Table 1 – *continued*

Name	Date	Detector	Mode	Exposure (ks)	RA (J2000)	Dec. (J2000)
MS1137.5+6625	1999 September 30	ACIS-I	VFAINT	103.8	11 40 22.4	66 08 15
ClJ1226.9+3332(1)	2003 January 27	ACIS-I	VFAINT	25.7	12 26 58.1	33 32 47
ClJ1226.9+3332(2)	2004 August 07	ACIS-I	VFAINT	26.3	12 26 58.1	33 32 47
CL1415.2+3612	2003 September 16	ACIS-I	VFAINT	75.1	14 15 11.2	36 12 02
3C186	2002 May 16	ACIS-S	VFAINT	15.4	07 44 17.5	37 53 17

Table 2. Clusters with regions of localized substructure that have been excluded or down-weighted in the analysis. Column 2 lists the position angles (PA) that have been excluded in the case of Abell 2390, RXJ1347.5−1145, MACS1427.3+4408 and MACSJ0744.9+3927. Column 3 lists the radii (in h_{70}^{-1} kpc) within which the spectral data have been down-weighted by including a systematic uncertainty of ±30 per cent in quadrature with the statistical errors on the temperature measurements.

Cluster	Excluded PA	Down-weighted r
Abell 1795	–	75
Abell 2029	–	30
Abell 478	–	15
PKS0745−191	–	55
Abell 1413	–	40
Abell 2204	–	75
Abell 383	–	40
RXJ1504.1−0248	–	80
Abell 2390	255–15	50
RXJ2129.6+0005	–	40
Zwicky 3146	–	240
Abell 2537	–	40
MACSJ2229.8−2756	–	40
MACSJ0947.2+7623	–	40
MACSJ1931.8−2635	–	40
MACSJ1115.8+0129	–	85
MACSJ1532.9+3021	–	40
RXJ1347.5−1145	90–190	–
MACSJ1621.6+3810	–	45
MACSJ1427.3+4408	160–280	–
MACSJ0744.9+3927	210–330	–

may together be used to determine the X-ray emitting gas mass and total mass profiles in the clusters. For this analysis, we have used an enhanced version of the Cambridge X-ray deprojection code described by e.g. White, Jones & Forman (1997). This method is particularly well suited to the present task in that it does not use parametric fitting functions for the X-ray temperature, gas density or surface brightness in measuring the mass; the use of such functions introduces strong priors that complicate the interpretation of results and, in particular, can lead to an underestimation of uncertainties. The only additional important assumption in the analysis is the choice of a Navarro, Frenk & White (1995, 1997; hereafter NFW) model to parametrize the total (luminous-plus-dark) mass distributions:

$$\rho(r) = \frac{\rho_{\rm c}(z)\delta_{\rm c}}{(r/r_{\rm s})\,(1 + r/r_{\rm s})^2}, \tag{1}$$

where $\rho(r)$ is the mass density, $\rho_{\rm c}(z) = 3H(z)^2/8\pi G$ is the critical density for closure at redshift z, $r_{\rm s}$ is the scale radius, c is the concentration parameter (with $c = r_{200}/r_{\rm s}$) and $\delta_{\rm c} = 200\ c^3/3[\ln(1 + c) - c/(1 + c)]$.[3] Schmidt & Allen (2007) show that the NFW model provides a good description of the mass distributions in the clusters studied here.

Given the observed surface brightness profile and a particular choice of parameters for the total mass profile, the deprojection code is used to predict the temperature profile of the X-ray gas. (In detail, the median model temperature profile determined from 100 Monte Carlo simulations for each mass model is used.) This model temperature profile is then compared with the observed spectral, deprojected temperature profile and the goodness of fit is calculated using the sum over all temperature bins:

$$\chi^2 = \sum_{\rm all\,bins} \left(\frac{T_{\rm obs} - T_{\rm model}}{\sigma_{\rm obs}} \right)^2, \tag{2}$$

where $T_{\rm obs}$ is the observed, spectral deprojected temperature profile and $T_{\rm model}$ is the model, rebinned to the same spatial scale. For each cluster, the mass parameters are stepped over a grid of values and the best-fitting values and uncertainties determined via χ^2 minimization techniques. The X-ray emitting gas density, pressure, entropy, cooling time and mass, and the integrated X-ray gas mass fraction, $f_{\rm gas}$, are then determined in a straightforward manner from the Monte Carlo simulations and χ^2 values at each grid point.

A number of systematic issues affect the accuracy of the $f_{\rm gas}$ measurements and their interpretation; these are discussed in detail in Section 4.2. In particular, our analysis incorporates allowances for effects associated with calibration and modelling uncertainties and non-thermal pressure support in the X-ray emitting gas, employing priors that span conservative ranges for the likely magnitudes of these effects.

Finally, for a number of the clusters, small but noticeable substructure is present at small radii. This is likely to result from interactions between the central radio sources and surrounding gas (e.g. Böhringer et al. 1993; Fabian et al. 2000, 2003a, 2005, 2006; Birzan et al. 2004; Dunn & Fabian 2004; Dunn, Fabian & Taylor 2005; Forman et al. 2005; Allen et al. 2006; Rafferty et al. 2006) and/or 'sloshing' of the X-ray emitting gas within the central potentials (e.g. Churazov et al. 2003; Markevitch et al. 2003; Ascasibar & Markevitch 2006). The regions affected by such substructure are listed in Table 2. A systematic uncertainty of ±30 per cent has been added in quadrature to all spectral results determined from these regions, leading to them having little weight in the mass analysis.

[3] Note that the outermost pressure, at the limit of the X-ray surface brightness profile, is fixed using an iterative method that ensures a smooth, power-law pressure gradient in these regions. The model temperature profiles, for radii spanned by the spectral data, are not sensitive to any reasonable choices for the outer pressures.

2.5 The stellar baryonic mass fraction

Observations of nearby and intermediate redshift clusters show that for clusters in the mass/temperature range studied here, the average mass fraction in stars (in galaxies and intracluster light combined) $f_{\rm star} \sim 0.16\, h_{70}^{0.5}\, f_{\rm gas}$ (Lin & Mohr 2004; see also White et al. 1993; Fukugita et al. 1998; Balogh et al. 2001).

For the present analysis, we ideally require the ratio $s = f_{\rm star}/f_{\rm gas}$ measured within r_{2500} for each cluster. However, such measurements are not yet available for the bulk of the clusters studied here. For hot, massive clusters, the relative contribution of the central dominant galaxy to the overall cluster light is less significant than for cooler, less massive systems (e.g. Lin & Mohr 2004). We have therefore assumed that the stellar mass fraction within r_{2500} is similar to that measured within the virial radius, i.e. $s = 0.16\, h_{70}^{0.5}$, but have both included a conservative 30 per cent Gaussian uncertainty in this value and allowed for evolution at the ± 20 per cent level, per unit redshift interval. Since the stellar mass accounts for only $\sim$14 per cent of the overall baryon budget within r_{2500} and less than 2 per cent of the total mass, these systematic uncertainties do not have a large effect on the overall error budget. A program to measure the evolution of the optical baryonic mass content of the largest relaxed clusters is underway.

3 THE X-RAY GAS MASS FRACTION MEASUREMENTS

3.1 New $f_{\rm gas}$ measurements

As mentioned above, in compiling the results on the X-ray gas mass fraction, $f_{\rm gas}$, we have adopted a canonical measurement radius of r_{2500}. The r_{2500} value for each cluster is determined directly from the *Chandra* data, with confidence limits calculated from the χ^2 grids. In general, the values are well matched to the outermost radii at which reliable temperature measurements can be made from the *Chandra* data, given systematic uncertainties associated with the background modelling.

Fig. 1(a) shows the observed $f_{\rm gas}(r)$ profiles for the six lowest redshift clusters in the sample, for the reference ΛCDM cosmology. Although some dispersion in the profiles is present, particularly at small radii, the profiles tend towards a common value at r_{2500}. Fitting the $f_{\rm gas}$ measurements at r_{2500} for the six lowest redshift systems with a constant value we obtain $f_{\rm gas} = 0.113 \pm 0.003$, with $\chi^2 = 4.3$ for five degrees of freedom. Fitting the results for all 42 clusters gives $f_{\rm gas} = 0.1104 \pm 0.0016$, with $\chi^2 = 43.5$ for 41 degrees of freedom.

Fig. 1(b) shows the $f_{\rm gas}(r/r_{2500})$ profiles for all 42 clusters in the sample. Fitting the data in the range 0.7–1.2r_{2500} with a power-law model, we measure $f_{\rm gas} = 0.1105 \pm 0.0005(r/r_{2500})^{0.214\pm0.022}$. Note that the error bars on the mean $f_{\rm gas}$ measurements quoted above reflect only the statistical uncertainties in these values. A systematic uncertainty of $\sim$10–15 per cent in the global, absolute $f_{\rm gas}$ normalization is also present due to uncertainties in e.g. instrument calibration, X-ray modelling and non-thermal pressure support; this must be accounted for in the determination of cosmological constraints (Section 4.2).

Table 3 summarizes the results on the X-ray gas mass fraction for each cluster measured at r_{2500}, together with the r_{2500} values, for the reference ΛCDM cosmology. Fig. 2 shows a comparison of the $f_{\rm gas}$ results, plotted as a function of redshift, for the reference ΛCDM cosmology and a flat, standard cold dark matter (SCDM) cosmology with $\Omega_{\rm m} = 1.0, h = 0.5$. Whereas the results for the ΛCDM cosmology appear consistent with the expectation of a constant $f_{\rm gas}(z)$ value from non-radiative simulations (e.g. Eke et al. 1998; Crain et al. 2007), as evidenced by the acceptable χ^2 value quoted above, the results for the reference SCDM cosmology indicate a clear, apparent drop in $f_{\rm gas}$ as the redshift increases. The χ^2 value obtained from a fit to the SCDM data with a constant model, $\chi^2 = 144$ for 41 degrees of freedom, shows that the SCDM cosmology is clearly inconsistent with a prediction that $f_{\rm gas}(z)$ should be constant.

Table 3 also lists the mass-weighted temperatures measured within r_{2500} for each cluster. Fig. 3 shows $f_{\rm gas}$ as a function of kT_{2500} for the reference ΛCDM cosmology. The dotted line in the figure shows the best-fitting power-law model, $f_{\rm gas}(r_{2500}) \propto kT_{2500}^{\alpha}$, which provides a good description of the data ($\chi^2 = 43.5$ for 40 degrees of freedom) and is consistent with a constant value ($\alpha = 0.005 \pm 0.058$). The solid lines shows the 2σ limits on the steepest and shallowest allowed power-law models. It is clear from the figure that $f_{\rm gas}$ is independent of temperature for the clusters in the present sample.

3.2 Comparison with previous $f_{\rm gas}$ results

Approximately 0.75 Ms of the $\sim$1.6 Ms of *Chandra* data used here were also included in the Allen et al. (2004) study. The current work includes a reanalysis of those data using improved calibration information, where available. The $f_{\rm gas}$ results from the two studies show

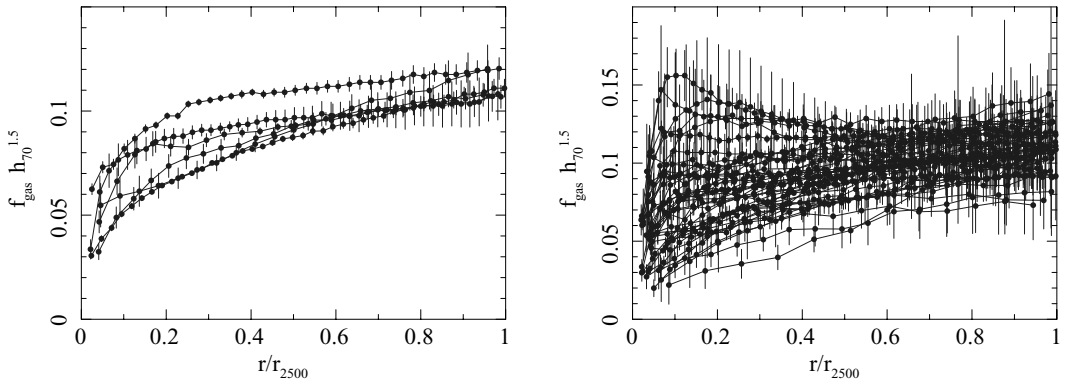

Figure 1. The X-ray gas mass fraction profiles for the ΛCDM reference cosmology ($\Omega_{\rm m} = 0.3, \Omega_\Lambda = 0.7, h = 0.7$) with the radial axes scaled in units of r_{2500}. Left-hand panel: Results for the six lowest redshift clusters with $z \lesssim 0.15$. Right-hand panel: Results for the entire sample. Note $f_{\rm gas}(r)$ is an integrated quantity and so error bars on neighbouring points in a profile are correlated.

Table 3. The redshifts, r_{2500} values, mean mass-weighted temperatures within r_{2500} and the X-ray gas mass fractions within r_{2500} for the reference ΛCDM cosmology. Error bars are statistical uncertainties and are quoted at the 68 per cent confidence level. A systematic uncertainty of ∼10–15 per cent is associated with the global, absolute normalization of the $f_{\rm gas}$ values due to uncertainties in instrument calibration, X-ray modelling and non-thermal pressure support (Section 4.2). The redshifts for the MACS clusters are from Ebeling et al. (2007, in preparation).

	z	$r_{2500}(h_{70}^{-1}\,\mathrm{kpc})$	kT_{2500}	$f_{\rm gas}\,h_{70}^{1.5}$
Abell 1795	0.063	570^{+18}_{-24}	6.51 ± 0.23	0.1074 ± 0.0075
Abell 2029	0.078	611^{+10}_{-13}	8.58 ± 0.44	0.1117 ± 0.0042
Abell 478	0.088	643^{+16}_{-15}	7.99 ± 0.43	0.1211 ± 0.0053
PKS0745−191	0.103	682^{+42}_{-41}	9.50 ± 1.13	0.1079 ± 0.0124
Abell 1413	0.143	599^{+17}_{-19}	7.80 ± 0.35	0.1082 ± 0.0058
Abell 2204	0.152	628^{+38}_{-24}	10.51 ± 2.54	0.1213 ± 0.0116
Abell 383	0.188	502^{+25}_{-23}	5.36 ± 0.23	0.0903 ± 0.0080
Abell 963	0.206	540^{+24}_{-27}	7.26 ± 0.28	0.1144 ± 0.0102
RXJ0439.0+0521	0.208	454^{+37}_{-25}	4.86 ± 0.45	0.0917 ± 0.0127
RXJ1504.1−0248	0.215	671^{+44}_{-33}	9.32 ± 0.59	0.1079 ± 0.0111
Abell 2390	0.230	662^{+42}_{-30}	11.72 ± 1.43	0.1257 ± 0.0110
RXJ2129.6+0005	0.235	507^{+65}_{-57}	7.38 ± 0.88	0.1299 ± 0.0299
Abell 1835	0.252	684^{+27}_{-26}	10.57 ± 0.62	0.1197 ± 0.0082
Abell 611	0.288	518^{+43}_{-30}	7.39 ± 0.48	0.1020 ± 0.0133
Zwicky 3146	0.291	679^{+66}_{-66}	8.27 ± 1.08	0.0943 ± 0.0163
Abell 2537	0.295	518^{+57}_{-33}	8.12 ± 0.78	0.0949 ± 0.0147
MS2137.3−2353	0.313	479^{+18}_{-10}	5.65 ± 0.30	0.1106 ± 0.0061
MACSJ0242.6−2132	0.314	478^{+29}_{-20}	5.51 ± 0.47	0.1268 ± 0.0131
MACSJ1427.6−2521	0.318	412^{+42}_{-37}	5.24 ± 0.77	0.1052 ± 0.0220
MACSJ2229.8−2756	0.324	414^{+41}_{-29}	5.42 ± 0.68	0.1452 ± 0.0265
MACSJ0947.2+7623	0.345	594^{+65}_{-49}	7.80 ± 0.69	0.1048 ± 0.0196
MACSJ1931.8−2635	0.352	581^{+131}_{-46}	7.49 ± 0.77	0.1193 ± 0.0266
MACSJ1115.8+0129	0.355	664^{+118}_{-108}	8.92 ± 1.31	0.0925 ± 0.0283
MACSJ1532.9+3021	0.363	543^{+45}_{-33}	7.69 ± 1.34	0.1280 ± 0.0162
MACSJ0011.7−1523	0.378	497^{+40}_{-27}	6.56 ± 0.37	0.1067 ± 0.0125
MACSJ1720.3+3536	0.391	520^{+39}_{-32}	8.11 ± 0.55	0.1153 ± 0.0151
MACSJ0429.6−0253	0.399	439^{+19}_{-24}	6.10 ± 0.58	0.1375 ± 0.0154
MACSJ0159.8−0849	0.404	597^{+33}_{-48}	10.62 ± 0.69	0.1097 ± 0.0160
MACSJ2046.0−3430	0.423	413^{+62}_{-50}	5.81 ± 1.02	0.1253 ± 0.0398
MACSJ1359.2−1929	0.447	458^{+91}_{-56}	6.73 ± 0.96	0.0845 ± 0.0290
MACSJ0329.7−0212	0.450	481^{+26}_{-23}	6.85 ± 0.45	0.1262 ± 0.0129
RXJ1347.5−1144	0.451	776^{+43}_{-31}	14.54 ± 1.08	0.0923 ± 0.0078
3C295	0.461	419^{+20}_{-15}	5.09 ± 0.42	0.1067 ± 0.0096
MACSJ1621.6+3810	0.461	496^{+53}_{-39}	9.15 ± 1.01	0.0954 ± 0.0172
MACS1427.3+4408	0.487	428^{+67}_{-36}	6.65 ± 1.40	0.1201 ± 0.0294
MACSJ1311.0−0311	0.494	461^{+30}_{-26}	6.07 ± 0.71	0.1066 ± 0.0168
MACSJ1423.8+2404	0.539	467^{+18}_{-14}	7.80 ± 0.44	0.1141 ± 0.0086
MACSJ0744.9+3927	0.686	466^{+40}_{-23}	8.67 ± 0.98	0.1151 ± 0.0140
MS1137.5+6625	0.782	435^{+84}_{-44}	6.89 ± 0.78	0.0716 ± 0.0235
ClJ1226.9+3332	0.892	521^{+123}_{-54}	11.95 ± 1.97	0.0769 ± 0.0198
CL1415.2+3612	1.028	278^{+33}_{-25}	5.59 ± 0.84	0.1086 ± 0.0262
3C186	1.063	292^{+54}_{-57}	5.62 ± 1.00	0.1340 ± 0.0777

excellent overall agreement: the new $f_{\rm gas}$ values are, on average, ∼6 per cent lower than those reported by Allen et al. (2004), a difference consistent with expectations given the modification to the effective area calibration described in Section 2.3.

LaRoque et al. (2006) present $f_{\rm gas}$ measurements for 38 X-ray luminous clusters, including 10 of the large, dynamically relaxed systems studied here. Their best-fitting results at r_{2500} are in good overall agreement with the present work, with their $f_{\rm gas}$ values being,

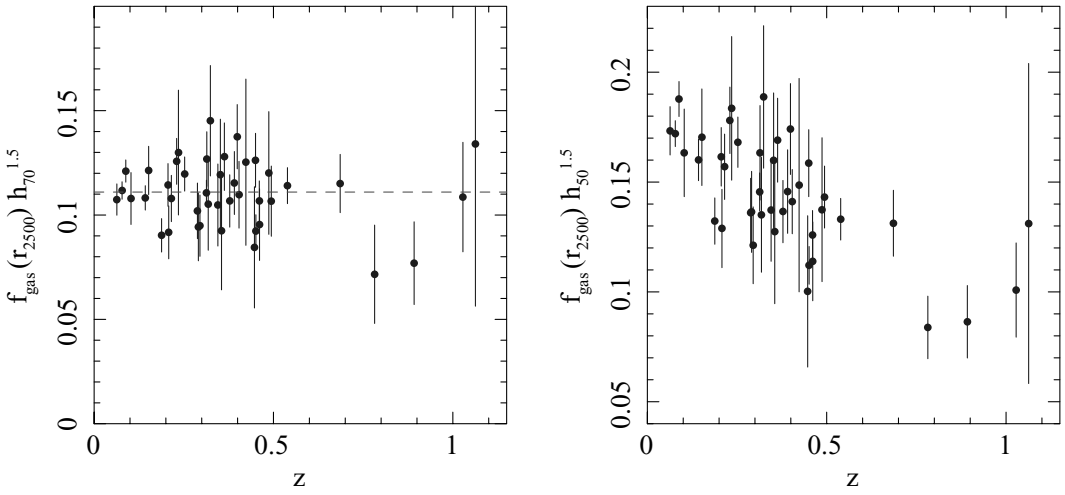

Figure 2. The apparent variation of the X-ray gas mass fraction measured within r_{2500} as a function of redshift for the (left-hand panel) reference ΛCDM and (right-hand panel) reference SCDM ($\Omega_m = 1.0, \Omega_\Lambda = 0.0, h = 0.5$) cosmologies. The plotted error bars are statistical rms 1σ uncertainties. The global, absolute normalization of the f_{gas} value should be regarded as uncertain at the ∼10–15 per cent level due to systematic uncertainties in instrument calibration, modelling and the level of non-thermal pressure support (Section 4.2).

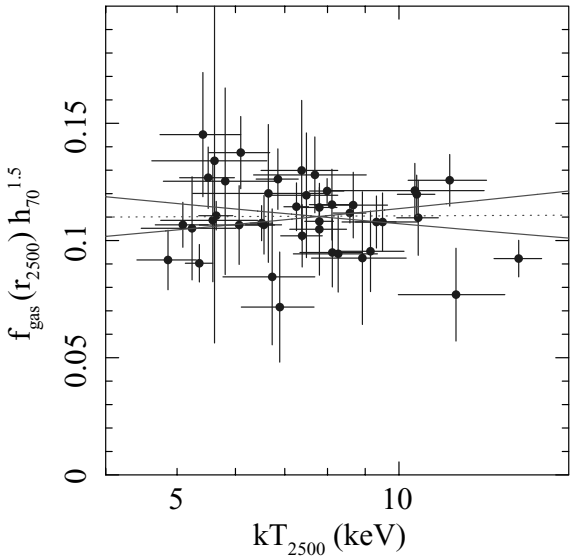

Figure 3. The X-ray gas mass fraction as a function of mass-weighted temperature measured within r_{2500} for the reference ΛCDM cosmology. The dotted line shows the best-fitting power-law model which provides a good description of the data ($\chi^2 = 43.5$ for 40 degrees of freedom) and is consistent with a constant value (slope $\alpha = 0.005 \pm 0.058$). The solid lines shows the 2σ limits on the slopes allowed by the data. The figure demonstrates that f_{gas} is essentially independent of temperature for the massive, dynamically relaxed clusters in the present sample.

on average, ∼6 per cent higher than those reported here, for the systems in common.

Pointecouteau et al. (2004) present an analysis of *XMM–Newton* data for Abell 478, for which they measure an f_{gas} value at r_{2500} of 0.13 ± 0.02, in good agreement with this work. These authors also report a value of 0.11 for Abell 1413, based on the data of Pratt & Arnaud (2002), which is consistent with the results reported here.

Vikhlinin et al. (2006) present f_{gas} measurements for 13 clusters of which six are in common with this study. On average, the Vikhlinin et al. (2006) f_{gas} results are ∼10 per cent lower than those reported here after correcting their values to the same reference ΛCDM cosmology.

We note that the statistical uncertainties on the f_{gas} measurements listed in Table 3 are, typically, larger than those reported by other authors. Two contributing factors to this difference are: (1) that the present analysis does not impose strong priors on the shapes of the temperature and density profiles in the clusters through the use of parametric models (the use of such parameterizations can lead to spuriously tight constraints in cases where they do not provide an adequate description of the data); and (2) the f_{gas} measurement errors reported here are marginalized over the uncertainties in all other parameters, including the uncertainties in r_{2500}.

4 COSMOLOGICAL ANALYSIS

4.1 Markov Chain Monte Carlo method

Our determination of cosmological parameters uses an MCMC method. We employ a modified version of the COSMOMC code[4] of Lewis & Bridle (2002; see Rapetti, Allen & Weller 2005; Rapetti et al. 2007 for details of the enhancements), which uses a Metropolis–Hastings MCMC algorithm to explore parameter space. We run the code on four to 16 processors simultaneously, creating multiple chains and using the message passing interface to dynamically update the proposal matrix based on the covariance of post-burn-in samples. This leads to a much faster convergence than would be obtained from a single chain run on a single compute node.

Convergence is assessed using the Gelman–Rubin criterion (Gelman & Rubin 1992). Convergence is deemed acceptable when the ratio of between-chain to mean-chain variances, R, satisfies $R - 1 < 0.1$. (We have also visually compared individual chains to ensure that consistent final results were obtained.) In general, our combined chains typically have lengths of at least 10^5 samples and have $R - 1 \ll 0.1$. (For the evolving-w models, $R - 1 \sim 0.1$.) Conservative burn-in periods of at least 10 000 samples were allowed for each chain.

[4] http://cosmologist.info/cosmomc/.

4.2 Analysis of the $f_{\rm gas}$ data: modelling and systematic allowances

The differences between the shapes of the $f_{\rm gas}(z)$ curves in Figs 2(a) and (b) reflect the dependence of the measured $f_{\rm gas}$ values on the assumed angular diameter distances to the clusters. Under the assumption (Section 1) that $f_{\rm gas}$ should, in reality, be approximately constant with redshift, as suggested by non-radiative simulations of large clusters (Eke et al. 1998; Crain et al. 2007; uncertainties in the predictions from simulations are discussed below) inspection of Fig. 2 would clearly favour the ΛCDM over the SCDM cosmology.

To determine constraints on cosmological parameters, it is not necessary to generate $f_{\rm gas}(z)$ data sets for every cosmology of interest and compare them to the expected behaviour. Rather, one can fit a single, reference $f_{\rm gas}(z)$ data set with a model that accounts for the expected apparent variation in $f_{\rm gas}(z)$ as the underlying cosmology is varied. We choose to work with the ΛCDM reference cosmology, although similar results can in principle be derived for other reference cosmologies.

The model fitted to the reference ΛCDM data is

$$f_{\rm gas}^{\Lambda{\rm CDM}}(z) = \frac{K A \gamma b(z)}{1+s(z)} \left(\frac{\Omega_{\rm b}}{\Omega_{\rm m}}\right) \left[\frac{d_{\rm A}^{\Lambda{\rm CDM}}(z)}{d_{\rm A}(z)}\right]^{1.5}, \quad (3)$$

where $d_{\rm A}(z)$ and $d_{\rm A}^{\Lambda{\rm CDM}}(z)$ are the angular diameter distances to the clusters in the current test model and reference cosmologies,

$$d_A = \frac{c}{H_0(1+z)\sqrt{\Omega_{\rm k}}} \sinh\left(\sqrt{\Omega_{\rm k}}\int_0^z \frac{{\rm d}z}{E(z)}\right), \quad (4)$$

with $E(z)$ defined as in Section 4.4. The factor A in equation (3) accounts for the change in angle subtended by r_{2500} as the underlying cosmology is varied[5]:

$$A = \left(\frac{\theta_{2500}^{\Lambda{\rm CDM}}}{\theta_{2500}}\right)^{\eta} \approx \left\{\frac{H(z)d_{\rm A}(z)}{[H(z)d_{\rm A}(z)]^{\Lambda{\rm CDM}}}\right\}^{\eta}. \quad (5)$$

Here, η is the slope of the $f_{\rm gas}(r/r_{2500})$ data in the region of r_{2500}, as measured for the reference ΛCDM cosmology. For simplicity, we use the best-fitting average slope of $\eta = 0.214 \pm 0.022$ determined from a fit to the whole sample over the range $0.7 < r/r_{2500} < 1.2$ (Section 3) and marginalize over the slope uncertainty. This angular correction factor, which is close to unity for all cosmologies and redshifts of interest, has not been employed in previous studies and, indeed, can be neglected without significant loss of accuracy for most work. Nevertheless, we include it here for completeness and note that its inclusion leads to slightly tighter constraints on dark energy than would otherwise be obtained.

The parameter γ in equation (3) models non-thermal pressure support in the clusters. Based on hydrodynamical simulations, Nagai et al. (2007a) estimate a bias of ∼9 per cent in $f_{\rm gas}$ measurements at r_{2500} for relaxed clusters. This bias originates primarily from subsonic motions in the intracluster gas and, as discussed by those authors (see also Section 5.3), can be regarded as an upper limit, given observational indications that the gas viscosity in real clusters appears likely to exceed that modelled in the simulations. For the large, relaxed clusters and measurement radii of interest here, non-thermal pressure support due to cosmic rays (Pfrommer et al. 2007) and magnetic fields (Dolag & Schindler 2000) is expected to be small. Based on these considerations, our default analysis assumes a uniform prior of $1.0 < \gamma < 1.1$, although we also consider the case where the non-thermal pressure support may be up to twice as large, i.e. $1.0 < \gamma < 1.2$.

The parameter $s(z) = s_0(1 + \alpha_{\rm s} z)$ in equation (3) models the baryonic mass fraction in stars. As discussed in Section 2.5, we include a 30 per cent Gaussian uncertainty on s_0, such that $s_0 = (0.16 \pm 0.05)\, h_{70}^{0.5}$, and a 20 per cent uniform prior on $\alpha_{\rm s}$, such that $-0.2 < \alpha_{\rm s} < 0.2$, allowing for evolution in the stellar baryonic mass fraction of ± 20 per cent per unit redshift interval.

The factor $b(z) = b_0(1 + \alpha_{\rm b} z)$ is the 'depletion' or 'bias' factor, i.e. the ratio by which the baryon fraction measured at r_{2500} is depleted with respect to the universal mean; such depletion is a natural consequence of the thermodynamic history of the gas. The non-radiative simulations of hot, massive clusters published by Eke et al. (1998; see also Crain et al. 2007) give $b_0 = 0.83 \pm 0.04$ at r_{2500}, and are consistent with no redshift evolution in b for $z < 1$. We use these simulations as a benchmark because other simulations that include cooling currently tend to significantly overproduce young stars in the largest galaxies (see e.g. Balogh et al. 2001), which is problematic for the prediction of $b(z)$. We note also the good agreement between the observed, scaled $f_{\rm gas}(r)$ profiles determined from the *Chandra* data and the $b(r)$ profiles for the three most relaxed clusters in the simulations of Eke et al. (1998; the red curves in

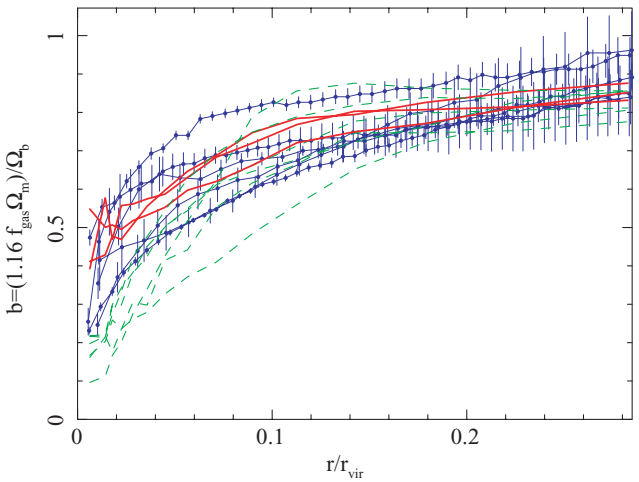

Figure 4. The X-ray depletion or bias factor, b (i.e. the enclosed baryon fraction relative to the universal value) as a function of radius, in units of the virial radius $r_{\rm vir}$, from the simulations of Eke et al. (1998). The simulated clusters have similar masses to the systems studied here. The results (at zero redshift) for the three most dynamically relaxed clusters in the simulations are shown as bold red curves. Less relaxed simulated clusters are shown as dashed green curves. The *Chandra* observations for the six lowest redshift clusters in the $f_{\rm gas}$ sample are plotted as blue circles, with error bars. (The *Chandra* profiles are identical to those shown in Fig. 1, but are scaled assuming $\Omega_{\rm m} = 0.27$, $\Omega_{\rm b} = 0.0413$ and $r_{2500} = 0.25\, r_{\rm vir}$.) The agreement between the observed and predicted profiles argues that the non-radiative simulations provide a reasonable approximation for the purpose of predicting the baryonic mass distributions.

[5] To see the origin of the correction factor A, recall that equation (3) predicts the $f_{\rm gas}$ value at the measurement radius in the reference ΛCDM cosmology. This measurement radius corresponds to a fixed angle $\theta_{2500}^{\Lambda{\rm CDM}}$ for each cluster, which will differ slightly from θ_{2500}, the angle corresponding to r_{2500} for that cluster in the current test cosmology. The mass contained within radius r_{2500}, $M_{2500} = 10^4 \pi r_{2500}^3 \rho_{\rm crit}/3$. Given that the temperature, and temperature and density gradients, in the region of θ_{2500} are likely to be approximately constant, the hydrostatic equation gives $M_{2500} \propto r_{2500}$. Thus, since $\rho_{\rm crit} = 3\,H(z)^2/8\pi G$, we have $r_{2500} \propto H(z)^{-1}$, and the angle spanned by r_{2500} at redshift z, $\theta_{2500} = r_{2500}/d_{\rm A} \propto (H(z)d_{\rm A})^{-1}$. Since the $f_{\rm gas}$ profiles follow a smooth power-law form in the region of θ_{2500}, the ratio of the model $f_{\rm gas}$ value at $\theta_{2500}^{\Lambda{\rm CDM}}$ to that at θ_{2500} can be described by equation (5).

Fig 4); this suggests that the non-radiative simulations provide a useful approximation for the purpose of predicting $b(z)$. (The profiles for the less relaxed simulated clusters are shown as dashed green curves in the figure.) Nevertheless, to account for systematic uncertainties in the predictions of $b(z)$, we include a conservative 20 per cent uniform prior on b_0, such that $0.65 < b_0 < 1.0$, and allow for moderate, systematic evolution in $b(z)$ over the observed redshift range, setting $-0.1 < \alpha_b < 0.1$. This encompasses a range of evolution allowed by recent simulations including various approximations to the detailed baryonic physics (e.g. Kay et al. 2004; Ettori et al. 2006; Crain et al. 2007; Nagai et al. 2007a).

The factor K in equation (3) is a 'calibration' constant that parametrizes residual uncertainty in the accuracy of the instrument calibration and X-ray modelling. Contributing factors include uncertainty in the instrument effective area, variations in element abundance ratios, modelling the effects of gas clumping and asphericity (the latter effects are expected to be small for large, relaxed clusters; Nagai et al. 2007a. See also Piffaretti, Jetzer & Schindler 2003; Gavazzi 2005). We conservatively include a 10 per cent Gaussian uncertainty in K to model the combined effect of these factors, such that $K = 1.0 \pm 0.1$. The small intrinsic dispersion in f_{gas} values (Section 5.3) means that Malmquist bias is expected to have a negligible effect on the derived cosmological parameters. Uncertainties associated with other systematic factors are expected to be negligible in comparison to the allowances listed above.

In cases where the *Chandra* f_{gas} data are not combined with CMB data, we include simple Gaussian priors on $\Omega_b h^2$ and h. Two separate sets of priors were used: 'standard' priors with $\Omega_b h^2 = 0.0214 \pm 0.0020$ (Kirkman et al. 2003) and $h = 0.72 \pm 0.08$ (Freedman et al. 2001), and 'weak' priors in which the nominal uncertainties were tripled to give $\Omega_b h^2 = 0.0214 \pm 0.0060$ and $h = 0.72 \pm 0.24$. In cases where the CMB data are included, no priors on $\Omega_b h^2$ or h are needed or used. The complete set of standard priors and allowances included in the f_{gas} analysis are summarized in Table 4.

Finally, we note how inspection of equation (3) can provide useful insight into the strength of the f_{gas} experiment. The pre-factors before the square brackets shows how the *normalization* of the $f_{gas}(z)$ curve is used to constrain Ω_m, given prior information on $\Omega_b, h, K, \gamma, b$ and s. The ratio of distances inside the square brackets (and to a small extent the angular correction factor) shows how the *shape* of the $f_{gas}(z)$ curve constrains the geometry of the Universe and therefore dark energy. The combination of information from both the normalization and shape *breaks the degeneracy* between Ω_m and the dark energy parameters in the distance equations.

Table 4. Summary of the standard systematic allowances and priors included in the *Chandra* f_{gas} analysis. The priors on $\Omega_b h^2$ and h (Freedman et al. 2001; Kirkman et al. 2003) are used when the CMB data are not included. We have also examined the case where the allowance for non-thermal pressure support has been doubled i.e. $1.0 < \gamma < 1.2$ (see text for details).

Cluster	Parameter	Allowance
Calibration/modelling	K	1.0 ± 0.1 (Gaussian)
Non-thermal pressure	γ	$1.0 < \gamma < 1.1$
Gas depletion: normalization	b_0	$0.65 < b_0 < 1.0$
Gas depletion: evolution	α_b	$-0.1 < \alpha_b < 0.1$
Stellar mass: normalization	s_0	0.16 ± 0.048 (Gaussian)
Stellar mass: evolution	α_s	$-0.2 < \alpha_s < 0.2$
$f_{gas}(r \sim r_{2500})$ slope	η	0.214 ± 0.022 (Gaussian)
Standard prior $\Omega_b h^2$	$\Omega_b h^2$	0.0214 ± 0.0020
Standard prior h	h	0.72 ± 0.08
Weak prior $\Omega_b h^2$	$\Omega_b h^2$	0.0214 ± 0.0060
Weak prior h	h	0.72 ± 0.24

4.3 Other data used in the analysis

In addition to the analysis of the *Chandra* f_{gas} data alone, we have examined the improved constraints on cosmological parameters that can be obtained through combination of the f_{gas} data with CMB and SNIa studies.

Our analysis of CMB observations uses the three-year *Wilkinson Microwave anisotropy Probe* (*WMAP*) temperature (TT) data for multipoles $l < 1000$ (Hinshaw et al. 2007; Spergel et al. 2007) and temperature-polarization (TE) data for $l < 450$ (Page et al. 2007). We use the October 2006 version of the *WMAP* likelihood code available from http://lambda.gsfc.nasa.gov/product/map/current/m_sw.cfm. Like most authors, we have ignored the small contribution to the TT data expected to arise from the Sunyaev–Z'eldovich (SZ) effect in clusters and groups (e.g. Komatsu & Seljak 2002) and do not account for gravitational lensing of the CMB (Lewis & Challinor 2006), which has a negligible effect on the derived cosmological parameters. To extend the analysis to higher multipoles (smaller scales), we also include data from the Cosmic Background Imager (Mason et al. 2003; Pearson et al. 2003), the Arcminute Cosmology Bolometer Array Receiver (Kuo et al. 2003) and BOOMERanG (Piacentini et al. 2005; Jones et al. 2006; Montroy et al. 2006), as incorporated into the current version of the COSMOMC code (Lewis & Bridle 2002). We use a modified version of CAMB (Lewis, Challinor & Lasenby 2000) to calculate CMB power spectra, which includes a consistent treatment of the effects of dark energy perturbations for evolving-w models (Rapetti et al. 2005; we assume that the sound speed in the dark energy fluid is equal to the speed of light).

Our analysis of SNIa data uses two separate supernova samples. In the first case, we use the compilation of Davis et al. (2007) which includes results from the ESSENCE survey (60 targets; Miknaitis et al. 2007; Wood-Vasey et al. 2007), the SNLS first-year data (57 targets; Astier et al. 2006), 45 nearby supernovae (Jha et al. 2007) and the 30 high-redshift supernovae discovered by *Hubble Space Telescope* (*HST*) and reported by Riess et al. (2007) for which a 'gold' rating was awarded. This sample includes 192 SNIa in total. The second supernova sample is the full 'gold' sample of Riess et al. (2007) which totals 182 SNIa, including the *HST*-discovered objects. For both samples we marginalize analytically over the absolute normalization of the distance moduli.

4.4 Dark energy models

We have considered three separate dark energy models in the analysis: (1) standard ΛCDM, for which the dark energy equation of state $w = -1$; (2) a model that allows any constant dark energy equation of state, including 'phantom' models with $w < -1$; (3) a model in which the dark energy equation of state is allowed to evolve as

$$w = \frac{w_{et} z + w_0 z_t}{z + z_t} = \frac{w_{et}(1-a)a_t + w_0(1-a_t)a}{a(1-2a_t) + a_t}, \quad (6)$$

where $a = 1/(1+z)$ is the scalefactor, w_0 and w_{et} are the equation of state at late (present day) and early times, and z_t and a_t are the redshift and scalefactor at the transition between the two, respectively (Rapetti et al. 2005; see also Chevallier & Polarski 2001; Linder 2003, 2007; Corasaniti et al. 2004). We employ a uniform prior on the transition scalefactor such that $0.5 < a_t < 0.95$. As

discussed by Rapetti et al. (2005), this model is both more general and more applicable to current data, which primarily constrain the properties of dark energy at redshifts $z < 1$, than models which impose a transition redshift $z = 1$, e.g. $w(a) = w_0 + w_a(1 - a)$.

Energy conservation of the dark energy fluid leads to an evolution of the energy density with scalefactor

$$\rho_{\rm de}(a) = \rho_{\rm de,0} a^{-3} {\rm e}^{-3\int_1^a \frac{w(a')}{a'} {\rm d}a'}, \quad (7)$$

where $\rho_{\rm de,0}$ is the energy density of the dark energy fluid today. Using the parameterization of equation (6) we obtain

$$\int_1^a \frac{w(a')}{a'} {\rm d}a' = w_{\rm et} \ln a + (w_{\rm et} - w_0) g(a; a_{\rm t}), \quad (8)$$

with

$$g(a; a_{\rm t}) = \left(\frac{1 - a_{\rm t}}{1 - 2a_{\rm t}}\right) \ln\left(\frac{1 - a_{\rm t}}{a(1 - 2a_{\rm t}) + a_{\rm t}}\right). \quad (9)$$

The Friedmann equation, which relates the first time derivative of the scalefactor of the Universe to the total density, can be conveniently expressed as $(\dot{a}/a)^2 = H(a)^2 = H_0^2 E(a)^2$, with

$$E(a) = \sqrt{\Omega_{\rm m} a^{-3} + \Omega_{\rm DE} f(a) + \Omega_{\rm k} a^{-2}}. \quad (10)$$

Here $\Omega_{\rm k}$ is the curvature, $\Omega_{\rm DE}$ is the dark energy density and $f(a)$ is its redshift dependence. (Note that we have ignored the density contributions from radiation and relativistic matter in this expression, although they are included in the analysis.) For our most general dark energy parameterization (equation 6)

$$f(a) = a^{-3(1+w_{\rm et})} {\rm e}^{-3(w_{\rm et} - w_0) g(a; a_{\rm t})}. \quad (11)$$

For ΛCDM cosmologies, the dark energy density is constant and $f(a) = 1$. For $w < -1$ the dark energy density increases with time. For constant w models with $w < -1/3$, dark energy accelerates the expansion of the Universe. The results from a purely kinematic modelling of the data, which does not rely on the Friedmann equation and is independent of the assumptions of general relativity, are discussed by Rapetti et al. (2007).

Our combined analysis of *Chandra* $f_{\rm gas}$, SNIa and CMB data therefore has up to 10 interesting parameters: the physical dark matter and baryon densities in units of the critical density, the curvature $\Omega_{\rm k}$, the ratio of the sound horizon to the angular diameter distance for the CMB (Kosowsky, Milosavljevic & Jimenez 2002), the amplitude of the scalar power spectrum, the scalar spectral index, the optical depth to reionization, and up to three parameters associated with the dark energy equation of state: $w_0, w_{\rm et}$ and $a_{\rm t}$. In all cases, we assume an absence of both tensor components and massive neutrinos and, for the analysis of the CMB data alone, include a wide uniform prior on the Hubble parameter, $0.2 < h < 2.0$. (Tests in which tensor components are included with ΛCDM models lead to similar results on dark energy, but take much longer to compute.)

5 CONSTRAINTS ON COSMOLOGICAL PARAMETERS

5.1 Constraints on $\Omega_{\rm m}$ from the low-z $f_{\rm gas}$ data

In the first case, we have used the *Chandra* $f_{\rm gas}$ data for only the six, lowest redshift clusters in the sample, with $z \lesssim 0.15$, to constrain the mean matter density of the Universe. The restriction to low-z clusters minimizes correlated uncertainties associated with the nature of the dark energy component (dark energy has only a very small effect on the space–time metric over this redshift range; we employ a broad uniform prior such that $0.0 < \Omega_\Lambda < 2.0$) and renders negligible uncertainties associated with the evolution of the depletion factor and stellar baryonic mass fraction ($\alpha_{\rm b}$ and $\alpha_{\rm s}$). Fig. 5 shows the marginalized constraints on $\Omega_{\rm m}$ for a ΛCDM model with free curvature, using the standard priors on $\Omega_{\rm b} h^2$ and h, for which we obtain a result of $\Omega_{\rm m} = 0.28 \pm 0.06$. The full set of conservative systematic allowances, as described in Table 4, were included.

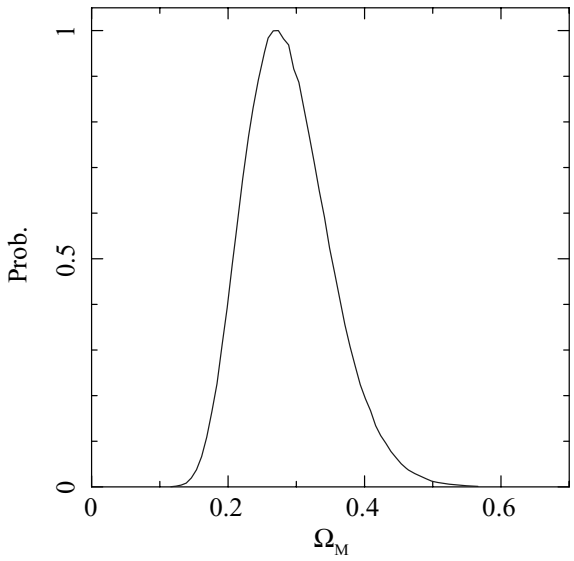

Figure 5. The marginalized constraints on $\Omega_{\rm m}$ from the *Chandra* $f_{\rm gas}$ data for the six lowest redshift clusters, using the non-flat ΛCDM model and standard priors on $\Omega_{\rm b} h^2$ and h. Uncertainties due to the evolution in b and s and the nature of the dark energy component are negligible in the analysis (although allowances for these uncertainties are included). We obtain a marginalized result $\Omega_{\rm m} = 0.28 \pm 0.06$ (68 per cent confidence limits).

The result on $\Omega_{\rm m}$ from the six lowest redshift clusters is in good agreement with that obtained for the whole sample, as discussed below. It is also consistent with the result on $\Omega_{\rm m}$ found from an analysis of all clusters *except* the six lowest redshift systems, $\Omega_{\rm m} = 0.29 \pm 0.06$, i.e. the six lowest redshift clusters do not dominate the $\Omega_{\rm m}$ constraints. Note that the error bars on $\Omega_{\rm m}$ are dominated by the widths of the priors on $\Omega_{\rm b} h^2$ and h and the magnitudes of the systematic allowances on K, b and γ, which are all at the ∼10–20 per cent level. In contrast, the statistical uncertainty in the normalization of the $f_{\rm gas}(z)$ curve is small (Section 3.1) and has a negligible impact on the $\Omega_{\rm m}$ results.

The result on $\Omega_{\rm m}$ is consistent with previous findings based on $f_{\rm gas}$ data (see references in Section 1) and independent constraints from the CMB (e.g. Spergel et al. 2007), galaxy redshift surveys (e.g. Eisenstein et al. 2005) and other leading cosmological data. Note that the agreement in cosmological parameters determined from the $f_{\rm gas}$ and CMB data argues against any unusual depletion of baryons within r_{2500} in hot, relaxed clusters (see e.g. the discussions in Ettori 2003; Afshordi et al. 2007; McCarthy, Bower & Balogh 2007).

5.2 Constraints on the ΛCDM model using the $f_{\rm gas}$ (+ CMB + SNIa) data

We next extended our analysis to measure $\Omega_{\rm m}$ and Ω_Λ for a non-flat ΛCDM model using the *Chandra* $f_{\rm gas}$ data for the full sample of 42 clusters. The results are shown as the red contours in Fig. 6. Using the systematic allowances summarized in Table 4 and the standard

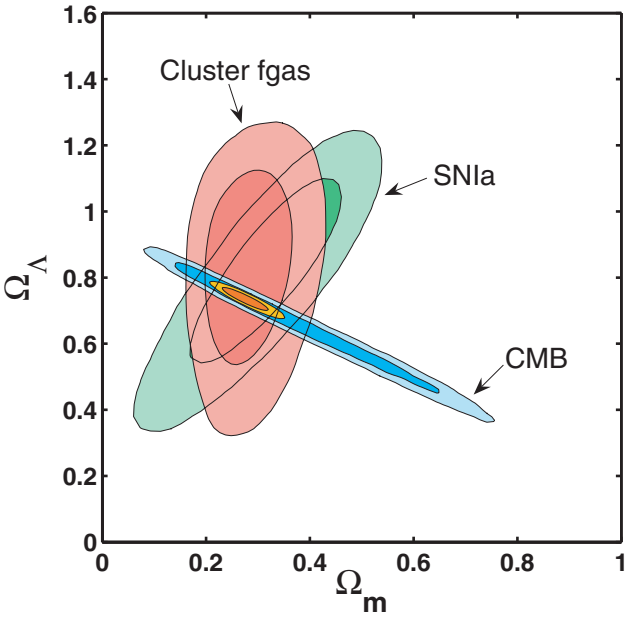

Figure 6. The 68.3 and 95.4 per cent (1 and 2 σ) confidence constraints in the (Ω_m, Ω_Λ) plane for the *Chandra* f_{gas} data (red contours; standard priors on $\Omega_b h^2$ and h are used). Also shown are the independent results obtained from CMB data (blue contours) using a weak, uniform prior on h ($0.2 < h < 2$), and SNIa data (green contours; the results for the Davis et al. 2007 compilation are shown). The inner, orange contours show the constraint obtained from all three data sets combined (no external priors on $\Omega_b h^2$ and h are used). A ΛCDM model is assumed, with the curvature included as a free parameter.

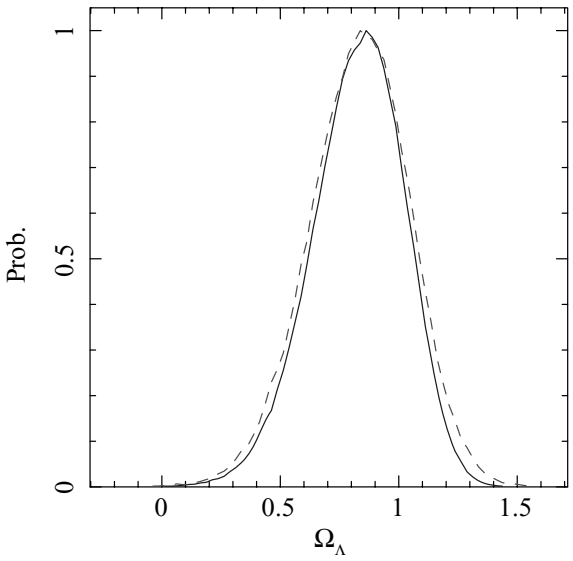

Figure 7. The marginalized constraints on Ω_Λ determined from the *Chandra* f_{gas} data using the non-flat ΛCDM model and standard (solid curve) and weak (dashed curve) priors on $\Omega_b h^2$ and h. The f_{gas} data provide a detection of the effects of dark energy at the ∼99.99 per cent confidence level.

priors on $\Omega_b h^2$ and h, we measure $\Omega_m = 0.27 \pm 0.06$ and $\Omega_\Lambda = 0.86 \pm 0.19$ (68 per cent confidence limits) with $\chi^2 = 41.5$ for 40 degrees of freedom. The low χ^2 value obtained is important and indicates that the model provides an acceptable description of the data (see Section 5.3 below). The result on Ω_m is in excellent agreement with that determined from the six lowest redshift clusters only (Section 5.1). The result is also consistent with the value reported by Allen et al. (2004) using the previous release of f_{gas} data, although the more conservative systematic allowances included here lead to the quoted uncertainties in Ω_m being larger by ∼50 per cent.

Fig. 7 shows the marginalized constraints on Ω_Λ obtained using both the standard and weak priors on $\Omega_b h^2$ and h. We see that using only the weak priors ($\Omega_b h^2 = 0.0214 \pm 0.0060, h = 0.72 \pm 0.24$), the f_{gas} data provide a clear detection of the effects of dark energy on the expansion of the Universe, with $\Omega_\Lambda = 0.86 \pm 0.21$: a model with $\Omega_\Lambda \leqslant 0$ is ruled out at ∼99.98 per cent confidence. (Using the standard priors on $\Omega_b h^2$ and h, a model with $\Omega_\Lambda \leqslant 0$ is ruled out at 99.99 per cent confidence; Table 5.) The significance of the detection of dark energy in the f_{gas} data is comparable to that of current SNIa studies (e.g. Riess et al. 2007; Wood-Vasey et al. 2007). The f_{gas} data provide strong, independent evidence for cosmic acceleration.

In contrast to the Ω_m constraints, the error budget for Ω_Λ includes significant contributions from both statistical and systematic sources. From the analysis of the full sample of 42 clusters using the standard priors on $\Omega_b h^2$ and h, we find $\Omega_\Lambda = 0.86 \pm 0.19$; the error bar comprises ± 0.15 statistical error and ± 0.12 systematic uncertainty. Thus, whereas improved measurements of Ω_m from the f_{gas} method will require additional information leading to tighter priors and systematic allowances, significant improvements in the precision of the dark energy constraints should be possible simply by gathering more data (e.g. doubling the present f_{gas} data set).

Fig. 6 also shows the constraints on Ω_m and Ω_Λ obtained from the CMB (blue contours) and SNIa (green contours) data (Section 4.3). The agreement between the results for the independent data sets is excellent and motivates a combined analysis. The inner, orange contours in Fig. 6 show the constraints on Ω_m and Ω_Λ obtained from the combined f_{gas} + CMB + SNIa data set. We obtain marginalized 68 per cent confidence limits of $\Omega_m = 0.275 \pm 0.033$ and $\Omega_\Lambda = 0.735 \pm 0.023$. Together, the f_{gas} + CMB + SNIa data also constrain the Universe to be close to geometrically flat: $\Omega_k = -0.010 \pm 0.011$. No external priors on $\Omega_b h^2$ and h are used in the analysis of the combined f_{gas} + CMB + SNIa data (see also Section 5.6).

Finally, we have examined the effects of doubling the allowance for non-thermal pressure support in the clusters, i.e. setting $1.0 < \gamma < 1.2$. For the analysis of the f_{gas} data alone, this boosts the best-fitting value of Ω_m by ∼5 per cent but leaves the results on dark energy unchanged. This can be understood by inspection of equation (3) and recalling that the constraint on Ω_m is determined primarily from the normalization of the f_{gas} curve, whereas the constraints on dark energy are driven by its shape (Section 4.2). For the combined f_{gas} + CMB + SNIa data set, doubling the width of the allowance on γ has a negligible impact on the results, since in this case the value of Ω_m is tightly constrained by the combination of data sets.

5.3 Scatter in the f_{gas} data

Hydrodynamical simulations suggest that the intrinsic dispersion in f_{gas} measurements for the largest, dynamically relaxed galaxy clusters should be small. Nagai et al. (2007a) simulate and analyse mock X-ray observations of galaxy clusters (including cooling and feedback processes), employing standard assumptions of spherical symmetry and hydrostatic equilibrium and identifying relaxed systems based on X-ray morphology in a similar manner to that employed here. For relaxed clusters, these authors find that f_{gas} measurements

Table 5. Summary of the constraints on cosmological parameters determined from the *Chandra* $f_{\rm gas}$ data and complementary data sets. Error bars reflect the combined statistical and systematic uncertainties, incorporating the allowances and priors described in Section 4.2. For the low-z $f_{\rm gas}$ data ($z < 0.15$), the constraint on $\Omega_{\rm m}$ is almost independent of the details of the dark energy component (Section 5.1). The SNIa(1) and SNIa(2) labels denote the supernovae samples of Davis et al. (2007) and Riess et al. (2007), respectively (Section 4.3).

Data	Model	$\Omega_{\rm b}\,h^2$, h priors	Cosmological constraints			
			$\Omega_{\rm m}$	$\Omega_{\rm DE}$	w_0	$w_{\rm et}$
low-z $f_{\rm gas}$	ΛCDM ($0 < \Omega_\Lambda < 2.0$)	Standard	0.28 ± 0.06	–	–	–
$f_{\rm gas}$	ΛCDM	Standard	0.27 ± 0.06	0.86 ± 0.19	–	–
$f_{\rm gas}$	ΛCDM	Weak	0.27 ± 0.09	0.86 ± 0.21	–	–
$f_{\rm gas}$ + CMB	ΛCDM	None	0.28 ± 0.06	0.73 ± 0.04	–	–
$f_{\rm gas}$ + CMB + SNIa(1)	ΛCDM	None	0.275 ± 0.033	0.735 ± 0.023	–	–
$f_{\rm gas}$	Constant w (flat)	Standard	0.28 ± 0.06	–	$-1.14^{+0.27}_{-0.35}$	–
$f_{\rm gas}$	Constant w (flat)	Weak	0.29 ± 0.09	–	$-1.11^{+0.31}_{-0.45}$	–
$f_{\rm gas}$+CMB	Constant w (flat)	None	0.243 ± 0.033	–	-1.00 ± 0.14	–
$f_{\rm gas}$ + CMB + SNIa(1)	Constant w (flat)	None	0.253 ± 0.021	–	-0.98 ± 0.07	–
$f_{\rm gas}$ + CMB + SNIa(1)	Constant w	None	0.310 ± 0.052	–	$-1.08^{+0.13}_{-0.19}$	–
$f_{\rm gas}$ + CMB + SNIa(1)	Evolving w (flat)	None	0.254 ± 0.022	–	$-1.05^{+0.31}_{-0.26}$	$-0.83^{+0.48}_{-0.43}$
$f_{\rm gas}$ + CMB + SNIa(1)	Evolving w	None	$0.29^{+0.09}_{-0.04}$	–	$-1.15^{+0.50}_{-0.38}$	$-0.80^{+0.70}_{-1.30}$
$f_{\rm gas}$ + CMB + SNIa(2)	Evolving w (flat)	None	0.287 ± 0.026	–	$-1.19^{+0.29}_{-0.35}$	$-0.33^{+0.18}_{-0.34}$

at r_{2500} are biased low by ∼9 per cent, with the bias primarily due to non-thermal pressure support provided by subsonic bulk motions in the intracluster gas. They measure an intrinsic dispersion in the $f_{\rm gas}$ measurements of ∼6 per cent, with an indication that the scatter may be even smaller for analyses limited to the hottest, relaxed systems with $kT \gtrsim 5$ keV. Nagai et al. (2007a) also suggest that the true scatter may be yet smaller if their simulations have underestimated the viscosity of the X-ray emitting gas.[6] In contrast, for *unrelaxed* simulated clusters, Nagai et al. (2007a) find that $f_{\rm gas}$ measurements are biased low by on average 27 per cent with an intrinsic dispersion of more than 50 per cent. Thus, the dispersion in $f_{\rm gas}$ measurements for unrelaxed clusters is expected to be an order of magnitude larger than for relaxed systems. This is in agreement with the measurement of very low intrinsic systematic scatter in the $f_{\rm gas}$ data for relaxed clusters reported here (see below) and the much larger scatter measured in previous works that included no such restriction to relaxed clusters. Earlier, non-radiative simulations by Eke et al. (1998) also argued for a small intrinsic scatter in $f_{\rm gas}$, at the few per cent level, for large, relaxed clusters (see also Crain et al. 2007). Likewise, Kay et al. (2004) measure a small intrinsic dispersion in $f_{\rm gas}$ measurements from simulations including cooling and moderate star formation.

The expectation of a small intrinsic dispersion in the $f_{\rm gas}$ measurements for hot, dynamically relaxed clusters is strikingly confirmed by the present data. Even without including the allowances for systematic uncertainties associated with γ, b_0, $\alpha_{\rm b}$, s and $\alpha_{\rm s}$ described in Table 4 (i.e. keeping only the 10 per cent systematic uncertainty on the overall normalization, as described by K) the best-fitting non-flat ΛCDM model gives an acceptable $\chi^2 = 41.9$ for 40 degrees of freedom, when fitting the full $f_{\rm gas}$ sample. (The χ^2 drops only to 41.5 with the full set of systematic allowances included; this small change in χ^2 illustrates the degeneracies between the systematic allowances and model parameters.) The acceptable χ^2 for the best-fitting model rules out the presence of significant intrinsic, systematic scatter in the current $f_{\rm gas}$ data. This absence of systematic scatter is observed despite the fact that the rms scatter in the $f_{\rm gas}$ data is only 15 per cent. Moreover, the rms scatter is dominated by those measurements with large statistical uncertainties; the weighted mean scatter of the $f_{\rm gas}$ data about the best-fitting ΛCDM model is only 7.2 per cent, which corresponds to only $7.2/1.5 = 4.8$ per cent in distance.

[6] Recent work on the morphologies of X-ray cavities and Hα filaments suggest a relatively high gas viscosity (low Reynolds number) in nearby cluster cores (Fabian et al. 2003a,b; Ruszkowski, Brüggen & Begelman 2004; Fabian et al. 2005; Reynolds et al. 2005).

5.4 Constraints on the constant w model using the $f_{\rm gas}$ (+ CMB + SNIa) data

We have next examined the ability of our data to constrain the dark energy equation of state parameter, w. In the first case, we examined a geometrically flat model in which w is constant with time. Fig. 8 shows the constraints in the $\Omega_{\rm m}$, w plane for this model using the *Chandra* $f_{\rm gas}$ data and standard priors/allowances (red contours), the CMB data (blue contours) and SNIa data (green contours). The different parameter degeneracies in the data sets are clearly evident. For the $f_{\rm gas}$ data alone, we measure $\Omega_{\rm m} = 0.28 \pm 0.06$ and $w = -1.14^{+0.27}_{-0.35}$.

The results for the three data sets shown in Fig. 8 are each, individually, consistent with the ΛCDM model ($w = -1$). The consistent nature of these constraints again motivates a combined analysis of the data, shown as the small, central (orange) contours. For the three data sets combined, we measure $\Omega_{\rm m} = 0.253 \pm 0.021$ and $w = -0.98 \pm 0.07$ (68 per cent confidence limits). No priors on $\Omega_{\rm b}\,h^2$ and h are required or used in the combined $f_{\rm gas}$ + CMB + SNIa analysis. The constraints on w from the combined data set are significantly tighter than 10 per cent.

We note that our analysis accounts for the effects of dark energy perturbations, which must exist for dark energy models other than ΛCDM; neglecting the effects of such perturbations can lead to spuriously tight constraints (see Rapetti et al. 2005 for details).

5.5 Constraints on the evolution of w from the combined $f_{\rm gas}$ + CMB + SNIa data

Fig. 9 shows the constraints on w_0 and $w_{\rm et}$ obtained from a combined analysis of $f_{\rm gas}$ + CMB + SNIa data using the general, evolving dark

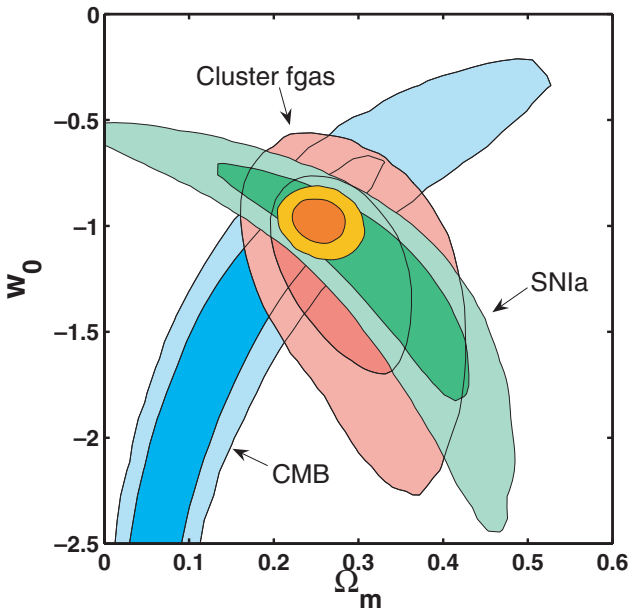

Figure 8. The 68.3 and 95.4 per cent (1 and 2σ) confidence constraints in the (Ω_m, w) plane obtained from the analysis of the *Chandra* f_{gas} data (red contours) using standard priors on $\Omega_b h^2$ and h. Also shown are the independent results obtained from CMB data (blue contours) using a weak, uniform prior on h ($0.2 < h < 2.0$) and SNIa data (green contours; Davis et al. 2007). The inner, orange contours show the constraint obtained from all three data sets combined: $\Omega_m = 0.253 \pm 0.021$ and $w = -0.98 \pm 0.07$ (68 per cent confidence limits). No external priors on $\Omega_b h^2$ and h are used when the data sets are combined. A flat cosmology with a constant dark energy equation of state parameter w is assumed.

energy model (equation 6) and assuming geometric flatness ($\Omega_k = 0$). The left- and right-hand panels show the results obtained for the two separate SNIa samples (Section 4.3). Using the Davis et al. (2007) SNIa compilation (left-hand panel), we find no evidence for evolution in the dark energy equation of state over the redshift range spanned by the data: the results on the dark energy equation of state at late and early times, $w_0 = -1.05^{+0.31}_{-0.26}$ and $w_{et} = -0.83^{+0.48}_{-0.43}$ (68 per cent confidence limits), are both consistent with a cosmological constant model ($w = -1$, constant). A similar conclusion is drawn by Davis et al. (2007) using SNIa + CMB + baryon acoustic oscillation (BAO) data.

We note, however, a hint of evolution in the dark energy equation of state when the Riess et al. (2007) 'gold' SNIa sample is used instead (right-hand panel of Fig. 9). In this case, the marginalized constraints on dark energy at late and early times, as defined in Section 4.4, differ at the 2–3σ level. Similar indications are also apparent in the analysis of the same SNIa (+ CMB + BAO) data by Riess et al. (2007). However, the analysis using the Davis et al. (2007) SNIa compilation (left-hand panel), which includes the high-quality, high-redshift *HST* supernovae from Riess et al. (2007) and which shows no suggestion of a departure from the ΛCDM model, argues that the hint of evolution in the right-hand panel of Fig. 9 may be systematic in origin (see also Conley et al. 2007; Riess et al. 2007 for discussions).

5.6 The degeneracy breaking power of the combined f_{gas} + CMB (+ SNIa) data

The degeneracy breaking power of the combined f_{gas} + CMB data set is evidenced in the left-hand panel of Fig. 10, which shows the constraints on Ω_m versus Ω_{DE} for a ΛCDM model with free curvature for the CMB data alone (blue contours) and the combined f_{gas} + CMB data set (orange contours). For the f_{gas} + CMB data, we measure $\Omega_m = 0.278^{+0.064}_{-0.050}$ and $\Omega_\Lambda = 0.732^{+0.040}_{-0.046}$ (68 per cent confidence limits), with the curvature $\Omega_k = -0.011^{+0.015}_{-0.017}$. As mentioned above, no external priors on $\Omega_b h^2$ and H_0 are required when the f_{gas} and CMB data are combined. The degeneracy breaking power of other combinations of data with the CMB is discussed by Spergel et al. (2007).

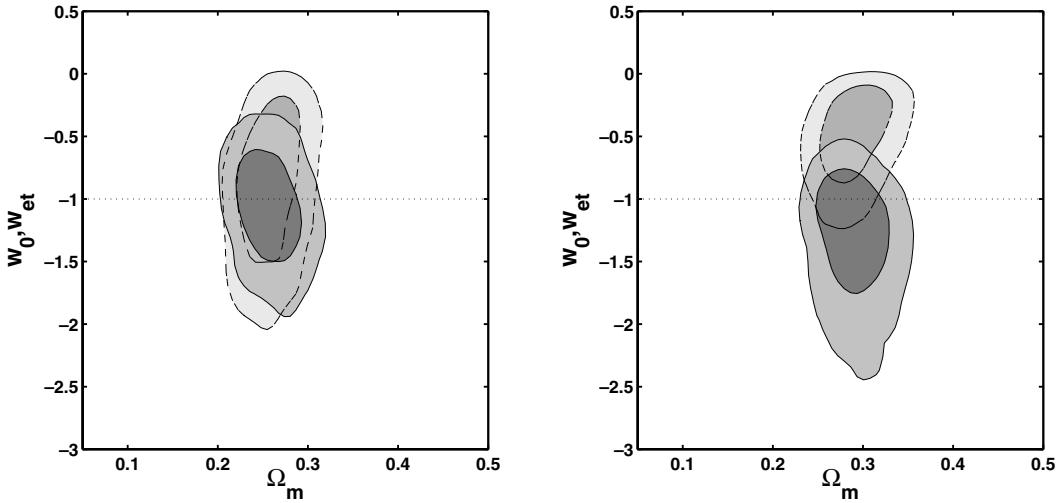

Figure 9. The 68.3 and 95.4 per cent confidence limits in the (Ω_m; w_0, w_{et}) plane determined from the f_{gas} + CMB + SNIa data using our most general dark energy model (equation 6) with the transition scalefactor marginalized over the range $0.5 < a_t < 0.95$. The solid, purple contours show the results on (Ω_m, w_0). The dashed, turquoise lines show the results on (Ω_m, w_{et}). The horizontal dotted line denotes the cosmological constant model ($w_0 = w_{et} = -1$). The left- and right-hand panels show the results obtained for the two SNIa samples: (left-hand panel) Davis et al. (2007) and (right-hand panel) Riess et al. (2007). A flat geometry ($\Omega_k = 0$) is assumed. The data provide no significant evidence for evolution in w and are consistent with the cosmological constant (ΛCDM) model ($w = -1$; Section 5.5).

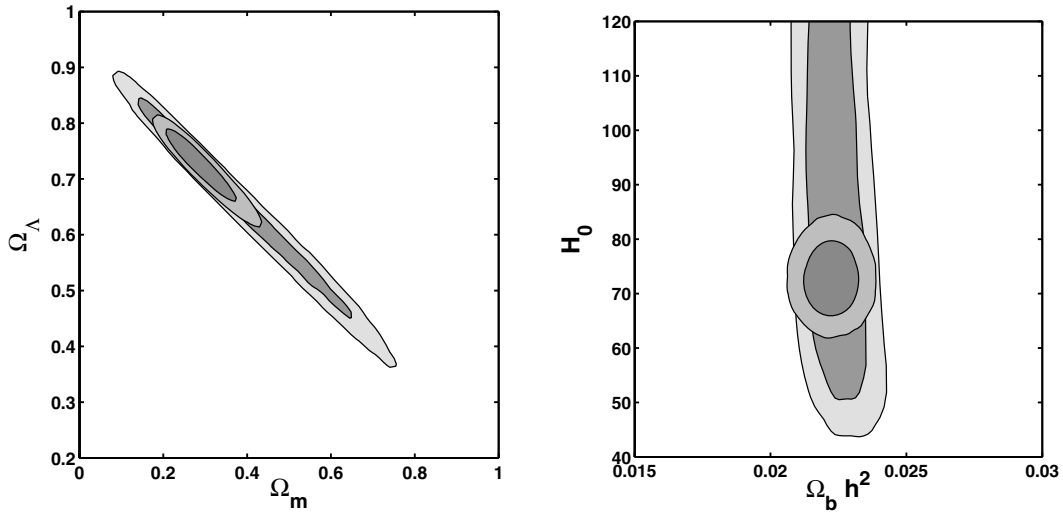

Figure 10. The degeneracy-breaking power of the $f_{\rm gas}$ + CMB data. Contours show the 68.3 and 95.4 per cent confidence limits determined from the CMB data alone (larger, blue contours) and combined $f_{\rm gas}$ + CMB data (smaller, orange contours). Left-hand panel: The constraints on $\Omega_{\rm m}$ and $\Omega_{\rm DE}$ for the ΛCDM model with the curvature included as a free parameter. Right-hand panel: The tight constraints on H_0 and $\Omega_{\rm b}\,h^2$ for the flat, constant w model, demonstrating why external priors on these two parameters are not required when the $f_{\rm gas}$ and CMB data are combined.

The right-hand panel of Fig. 10 shows the constraints on the Hubble constant, H_0, and mean baryon density, $\Omega_{\rm b}\,h^2$, determined using the flat, constant w model for the CMB data alone (blue contours) and the combined $f_{\rm gas}$ + CMB data set (orange contours). The improvement in the constraints on these parameters determined from the $f_{\rm gas}$ + CMB data over the CMB data alone is substantial. The tight constraints for the $f_{\rm gas}$ + CMB data, $H_0 = 72.5 \pm 4.6\,{\rm km\,s^{-1}\,Mpc^{-1}}$ and $\Omega_{\rm b}\,h^2 = 0.0223 \pm 0.0007$, demonstrate clearly why external priors on these two parameters are not required when the $f_{\rm gas}$ and CMB data are combined. Indeed, the constraints on H_0 and $\Omega_{\rm b}\,h^2$ obtained from the $f_{\rm gas}$ + CMB data are significantly tighter than the external priors on these parameters that are employed when the $f_{\rm gas}$ data are used alone (Table 4). Similar constraints on H_0 and $\Omega_{\rm b}\,h^2$ are presented by the *WMAP* team (Spergel et al. 2007) for flat ΛCDM models using various data combinations.

Fig. 11 shows the constraints on the dark energy equation of state obtained from an analysis of the combined $f_{\rm gas}$ + CMB + SNIa data set where the curvature is also included as a free parameter. The marginalized results for the constant w model (left-hand panel), $w = -1.08^{+0.13}_{-0.19}$ and $\Omega_{\rm k} = -0.024^{+0.022}_{-0.018}$, are comparable to those of Spergel et al. (2007; see their fig. 17) from a combined analysis of CMB, SNIa and Galaxy Redshift Survey data. The constraints for the non-flat evolving w model (right-hand panel), though weaker than those for the flat model (Fig. 9), remain interesting and are also consistent with a cosmological constant. As discussed by Rapetti et al. (2005; see also Spergel et al. 2007), such results demonstrate

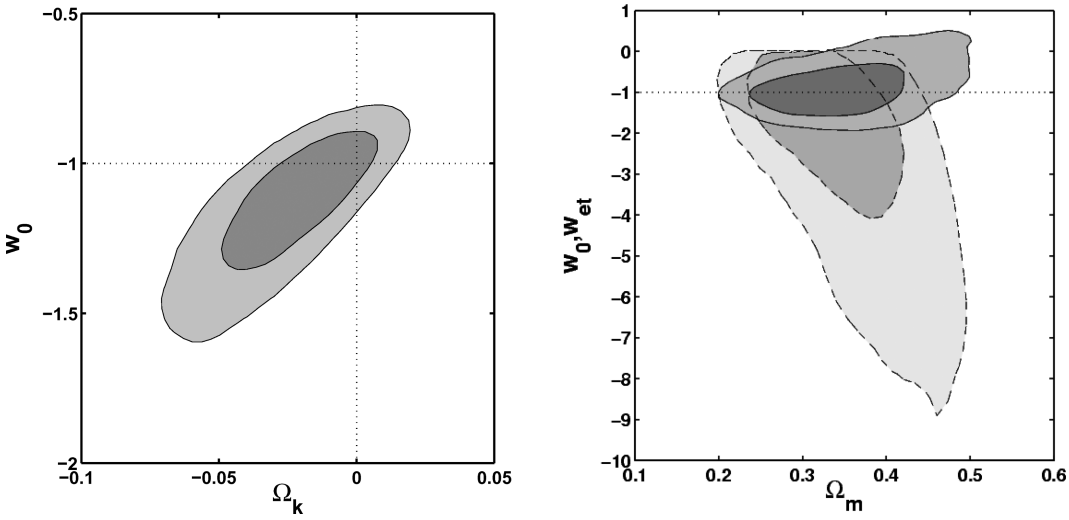

Figure 11. Left-hand panel: The 68.3 and 95.4 per cent confidence limits on the dark energy equation of state and curvature from the analysis of the $f_{\rm gas}$ + CMB + SNIa data using the non-flat, constant w model. The SNIa compilation of Davis et al. (2007) has been used. The horizontal and vertical dotted lines denote the loci for cosmological constant models and geometric flatness, respectively, both of which are consistent with the data. Right-hand panel: The 68.3 and 95.4 per cent confidence limits in the ($\Omega_{\rm m}$; w_0, $w_{\rm et}$) plane determined from the $f_{\rm gas}$ + CMB + SNIa data for the general dark energy model (equation 6) with the curvature also included as a free parameter. Other details are as in the left-hand panel of Fig. 9.

the power of the $f_{\rm gas}$ + CMB + SNIa data to constrain the properties of dark energy without the need to assume that the Universe is flat.

Using the non-flat evolving w model but fixing the transition redshift $z_{\rm t} = 1$ in equation (6), we recover the model used by the Dark Energy Task Force (DETF) to assess the power of future dark energy experiments. The combination of current $f_{\rm gas}$ + CMB + SNIa data provides a DETF figure of merit ∼2.

6 DISCUSSION

The new *Chandra* $f_{\rm gas}$ results and analysis presented here build upon those of Allen et al. (2004) and Rapetti et al. (2005). The present study includes 16 more objects, approximately twice as much *Chandra* data and extends the study beyond a redshift of 1. Our analysis includes a comprehensive and conservative treatment of systematic uncertainties (Section 4.2; see also Table 4). Allowances for such uncertainties are easily incorporated into the MCMC analysis.

As with SNIa studies, the $f_{\rm gas}$ data constrain dark energy via its effects on the distance–redshift relation to a well-defined source population – in this case, the largest, dynamically relaxed galaxy clusters – using measurements of a 'standard' astrophysical quantity – the ratio of baryonic-to-total mass in the clusters. Our results provide a clear and independent detection of the effects of dark energy on the expansion of the Universe at ∼99.99 per cent confidence for a standard non-flat ΛCDM model, an accuracy comparable to that obtained from current SNIa work (e.g. Astier et al. 2006; Miknaitis et al. 2007; Riess et al. 2007; Wood-Vasey et al. 2007). Like SNIa studies, the $f_{\rm gas}$ data trace the evolution of dark energy over the redshift range $0 < z < 1$, where it grows to dominate the overall energy density of the Universe. Our results for the $f_{\rm gas}$ data alone, and the combination of $f_{\rm gas}$ + CMB + SNIa data, show that this growth is consistent with that expected for models in which the dark energy is a cosmological constant ($w = -1$).

Despite some clear similarities, important complementary differences between the $f_{\rm gas}$ and SNIa experiments exist. In the first case, the physics of the astrophysical objects – large, relaxed galaxy clusters and SNIa – are very different; the fact that such similar cosmological results are obtained from the distance–redshift information for these separate source populations is reassuring. Future studies, combining the two techniques but using larger target samples, should open the possibility for precise distance–redshift measurements and good control of systematic uncertainties, employing both kinematic and dynamical analyses (e.g. Rapetti et al. 2007; Riess et al. 2007, and references therein).

An important strength of the $f_{\rm gas}$ method is the tight constraint on $\Omega_{\rm m}$ provided by the normalization of the $f_{\rm gas}$ curve; this breaks the degeneracy between the mean matter density and dark energy density inherent in the distance measurements. Our result on $\Omega_{\rm m}$ is consistent with a host of previous X-ray studies (Section 1).

A further strength, which is of relevance when considering observing strategies for future dark energy work, is the small intrinsic dispersion in the $f_{\rm gas}$ distance measurements. SNIa studies have established the presence of a systematic scatter of ∼7 per cent in distance measurements for individual SNIa using high-quality data (Jha et al. 2007; see also e.g. Riess et al. 2004; Astier et al. 2006; Riess et al. 2007; Wood-Vasey et al. 2007). In contrast, systematic scatter remains undetected in the present *Chandra* $f_{\rm gas}$ data for hot, relaxed clusters, despite the fact that the weighted mean *statistical* scatter in $f_{\rm gas}$ data corresponds to only ∼5 per cent in distance. This small systematic scatter for large, dynamically relaxed clusters (identified as relaxed on the basis of their X-ray morphologies) is consistent with the predictions from hydrodynamical simulations (e.g. Nagai et al. 2007a), although the results for both observed and simulated clusters are, at present, based on relatively small samples and more data are required. We stress that such small systematic scatter is neither expected nor observed in studies where a restriction to morphologically relaxed clusters is *not* employed, e.g. compare the small scatter measured here with the much larger scatter observed in the studies of LaRoque et al. (2006) and Ettori et al. (2003); see also Nagai et al. (2007a). The restriction to the hottest, relaxed clusters, for which $f_{\rm gas}$ is independent of temperature (Fig. 3) also simplifies the determination of cosmological parameters.

As mentioned above, the allowances for systematic uncertainties included in the analysis are relatively conservative. Much progress is expected over the coming years in refining the ranges of these allowances, both observationally and through improved simulations. As discussed in Sections 5.1 and 5.2, a reduction in the size of the required systematic allowances will tighten the cosmological constraints. Improved numerical simulations of large samples of massive clusters, including a more complete treatment of star formation and feedback physics that reproduces both the observed optical galaxy luminosity function and cluster X-ray properties, will be of major importance. Progress in this area has been made (e.g. Bialek et al. 2001; Muanwong et al. 2002; Ettori et al. 2004; Kay et al. 2004; Kravtsov, Nagai & Vikhlinin 2005; Ettori et al. 2006; Rasia et al. 2006; Nagai et al. 2007a; Nagai, Kravtsov & Vikhlinin 2007b), though more work remains. In particular, this work should improve the predictions for $b(z)$. Further deep X-ray and optical observations of nearby clusters will provide better constraints on the viscosity of the cluster gas. Improved optical/near infrared observations of clusters should pin down the stellar mass fraction in galaxy clusters and its evolution.

Ground and space-based gravitational lensing studies will provide important, independent constraints on the mass distributions in clusters; a large programme using the Subaru telescope and *HST* is underway, as is similar work by other groups (e.g. Hoekstra 2007). Follow-up observations of the SZ effect will also provide additional, independent constraining power in the measurement of cosmological parameters (the combination of direct observations of the SZ effect using radio/submillimetre data and the prediction of this effect from X-ray data provides an additional constraint on absolute distances to the clusters, e.g. Molnar, Birkinshaw & Mushotzky 2002; Schmidt, Allen & Fabian 2004; Bonamente et al. 2006 and references therein). Moreover, the independent constraints provided by the SZ observations should allow a reduction of the priors required in future work (e.g. Rapetti & Allen 2007).

In the near future, continuing programmes of *Chandra* and *XMM–Newton* observations of known, X-ray luminous clusters should allow important progress to be made, both by expanding the $f_{\rm gas}$ sample (e.g. *Chandra* snapshot observations of the entire MACS sample; Ebeling et al. 2001, 2007) and through deeper observations of the current target list. The advent of new, large area SZ surveys (e.g. Ruhl et al. 2004) will soon provide important new target lists of hot, X-ray luminous high-redshift clusters. A new, large area X-ray survey such as that proposed by the Spectrum-RG/eROSITA project[7] could make a substantial contribution, finding hundreds of suitable systems at high redshifts.

Looking a decade ahead, the Constellation-X Observatory (Con-X)[8] and, later, *XEUS*[9] offer the possibility to carry out

[7] http://www.mpe.mpg.de/projects.html \ #erosita.
[8] http://constellation.gsfc.nasa.gov/.
[9] http://www.rssd.esa.int/index.php?project=XEUS.

precise studies of dark energy using the $f_{\rm gas}$ technique. As discussed by Rapetti & Allen (2007; see also Rapetti et al. 2006), the large collecting area and combined spatial/spectral resolving power of Con-X should permit precise $f_{\rm gas}$ measurements with $\sim$5 per cent accuracy for large samples ($\gtrsim 500$) of hot, massive clusters ($kT \gtrsim 5\,{\rm keV}$) spanning the redshift range $0 < z < 2$ (typical redshift $z \sim 0.5$). The predicted constraints on dark energy from such an experiment, assuming Planck priors (Albrecht et al. 2006), have a DETF figure of merit $\gtrsim$20, which is comparable to other leading proposed dark energy techniques such as SNIa, cluster number counts, weak lensing and BAO studies. The high spectral resolution offered by the Con-X calorimeters will also permit precise measurements of bulk motions and viscosity in the cluster gas, addressing directly one of the main sources of systematic uncertainty in the method.

An ASCII table containing the redshift and $f_{\rm gas}(z)$ data is available at http://xoc.stanford.edu or from the authors on request. The analysis code, in the form of a patch to COSMOMC, will be made available at a later date.

ACKNOWLEDGMENTS

We thank Sarah Church, Vince Eke, Bob Kirshner, Gary Mamon, Herman Marshall, Rich Mushotzky, Jerry Ostriker, Harvey Tananbaum, Alexey Vikhlinin, Jochen Weller and Nick White for discussions over the course of this work. We also thank Antony Lewis for help with COSMOMC. The computational analysis presented here was carried out using the KIPAC XOC compute cluster at the Stanford Linear Accelerator Centre (SLAC). We acknowledge support from the National Aeronautics and Space Administration through *Chandra* Award Numbers DD5-6031X, GO2-3168X, GO2-3157X, GO3-4164X, GO3-4157X and G07-8125X, issued by the *Chandra* X-ray Observatory Centre, which is operated by the Smithsonian Astrophysical Observatory for and on behalf of the National Aeronautics and Space Administration under contract NAS8-03060. This work was supported in part by the US Department of Energy under contract number DE-AC02-76SF00515.

REFERENCES

Afshordi N., Lin Y.-T., Nagai D., Sanderson A. J. R., 2007, MNRAS, 378, 293
Albrecht A. et al., 2006, Report of the Dark Energy Task Force, preprint (astro-ph/0609591)
Allen S. W., Fabian A. C., Johnstone R. M., White D. A., Daines S. J., Edge A. C., Stewart G. C., 1993, MNRAS, 262, 901
Allen S. W., Schmidt R. W., Fabian A. C., 2002a, MNRAS, 334, L11
Allen S. W., Schmidt R. W., Fabian A. C., 2002b, MNRAS, 335, 256
Allen S. W., Schmidt R. W., Fabian A. C., Ebeling H., 2003, MNRAS, 342, 287
Allen S. W., Schmidt R. W., Ebeling H., Fabian A. C., van Speybroeck L., 2004, MNRAS, 353, 457
Allen S. W., Dunn R. J. H., Fabian A. C., Taylor G. B., Reynolds C. S., 2006, MNRAS, 372, 21
Arnaud K. A., 1996, in Jacoby G., Barnes J., eds, ASP Conf. Ser. Vol. 101, Astronomical Data Analysis Software and Systems V. Astron. Soc. Pac., San Francisco, p. 17
Ascasibar Y., Markevitch M., 2006, ApJ, 650, 102
Astier P. et al., 2006, A&A, 447, 31
Balogh M. L., Pearce F. R., Bower R. G., Kay S. T., 2001, MNRAS, 326, 1228
Balucinska-Church M., McCammon D., 1992, ApJ, 400, 699
Bialek J. J., Evrard A. E., Mohr J. J., 2001, ApJ, 555, 597
Birzan L., Rafferty D. A., McNamara B. R., Wise M. W., Nulsen P. E. J., 2004, ApJ, 607, 800
Böhringer H., Voges W., Fabian A. C., Edge A. C., Neuman D. M., 1993, MNRAS, 264, 25
Bonamente M., Joy M. K., LaRoque S. J., Carlstrom J. E., Reese E. D., Dawson K. S., 2006, ApJ, 647, 25
Borgani S. et al., 2004, MNRAS, 348, 1078
Briel U. G., Henry J. P., Böhringer H., 1992, A&A, 259, L31
Buote D. A., Tsai J. C., 1995, ApJ, 452, 522
Buote D. A., Tsai J. C., 1996, ApJ, 458, 27
Chevallier M., Polarski D., 2001, Int. J. Mod. Phys. D, 10, 213
Churazov E., Forman W., Jones C., Böhringer H., 2003, ApJ, 590, 225
Cole S. et al., 2005, MNRAS, 362, 505
Conley A., Carlberg R. G., Guy J., Howell D. A., Jha S., Riess A. G., Sullivan M., 2007, ApJ, 664, L13
Corasaniti P. S., Kunz M., Parkinson D., Copeland E. J., Bassett B. A., 2004, Phys. Rev. D., 70, 083006
Crain R. A., Eke V. R., Frenk C. S., Jenkins A. J., McCarthy I. G., Navarro J. F., Pearce F. R., 2007, MNRAS, 377, 41
David L. P., Jones C., Forman W., 1995, ApJ, 445, 578
Davis T. M. et al., 2007, ApJ, 666, 716
Dickey J. M., Lockman F. J., 1990, ARA&A, 28, 215
Dolag K., Schindler S., 2000, A&A, 364, 491
Dunn R. J. H., Fabian A. C., 2004, MNRAS, 355, 862
Dunn R. J. H., Fabian A. C., Taylor G. B., 2005, MNRAS, 364, 1343
Ebeling H., Edge A. C., Henry J. P., 2001, ApJ, 553, 668
Ebeling H., Barret E., Donovan D., Ma C.-J., Edge A. C., van Speybroeck L., 2007, ApJ, 661, L33
Eisenstein D. J. et al., 2005, ApJ, 633, 560
Eke V. R., Navarro J. F., Frenk C. S., 1998, ApJ, 503, 569
Ettori S., 2003, MNRAS, 344, L13
Ettori S., Fabian A. C., 1999, MNRAS, 305, 834
Ettori S., Tozzi P., Rosati P., 2003, A&A, 398, 879
Ettori S. et al., 2004, MNRAS, 354, 111
Ettori S., Dolag K., Borgani S., Murante G., 2006, MNRAS, 365, 1021
Evrard A. E., 1997, MNRAS, 292, 289
Fabian A. C., 1991, MNRAS, 253, L29
Fabian A. C. et al., 2000, MNRAS, 318, L65
Fabian A. C. et al., 2003a, MNRAS, 344, L43
Fabian A. C., Sanders J. S., Crawford C. S., Consilice C. J., Gallagher J. S., Wyse R. F. G., 2003b, MNRAS, 344, L48
Fabian A. C., Reynolds C. S., Taylor G. B., Dunn R. J. H., 2005, 363, 891
Fabian A. C., Sanders J. S., Taylor G. B., Allen S. W., Crawford C. S., Johnstone R. M., Iwasawa K., 2006, MNRAS, 366, 417
Forman W. et al., 2005, ApJ, 635, 894
Freedman W. et al., 2001, ApJ, 553, 47
Frenk C. S. et al., 1999, ApJ, 525, 554
Fukugita M., Hogan C. J., Peebles P. J. E., 1998, ApJ, 503, 518
Gavazzi R., 2005, A&A, 443, 793
Gelman A., Rubin D. B., 1992, Stat. Sci., 7, 457
Grego L., Carlstrom J. E., Reese E. D., Holder G. P., Holzapfel W. L., Joy M. K., Mohr J. J., Patel S., 2001, ApJ, 552, 2
Hinshaw G. et al., 2007, ApJS, 170, 288
Hoekstra H., 2007, MNRAS, 379, 317
Jeltema T. E., Canizares C. R., Bautz M. W., Buote D. A., 2005, ApJ, 624, 606
Jha S., Riess A. G., Kirshner R. P., 2007, ApJ, 659, 122
Jones W. C. et al., 2006, ApJ, 647, 823
Kaastra J. S., Mewe R., 1993, Legacy, 3, 16
Kay S. T., Thomas P. A., Jenkins A., Pearce F. R., 2004, MNRAS, 355, 1091
Kirkman D., Tytler D., Suzuki N., O'Meara J. M., Lubin D., 2003, ApJS, 149, 1
Komatsu E., Seljak U., 2002, MNRAS, 336, 1256
Kosowsky A., Milosavljevic M., Jimenez R., 2002, Phys. Rev. D, 66, 063007
Kravtsov A. V., Nagai D., Vikhlinin A. A., 2005, ApJ, 625, 588
Kuo C. L. et al., 2003, ApJ, 600, 32
Lahav O., Lilje P. B., Primack J. R., Rees M. J., 1991, MNRAS, 251, 128
LaRoque S. J., Bonamente M., Carlstrom J. E., Joy M. K., Nagai D., Reese E. D., Dawson K. S., 2006, ApJ, 652, 917
Lewis A., Bridle S., 2002, Phys. Rev. D, 66, 103511

Lewis A., Challinor A., 2006, Phys. Rep., 429, 1
Lewis A., Challinor A., Lasenby A., 2000, ApJ, 538, 473
Liedhal D. A., Osterheld A. L., Goldstein W. H., 1995, ApJ, 438, L115
Lin Y.-T., Mohr J. J., 2004, ApJ, 617, 879
Lin Y.-T., Mohr J. J., Stanford S. S., 2003, ApJ, 591, 794
Linder E. V., 2003, Phys. Rev. Lett., 90, 091301
Linder E. V., 2007, preprint (astro-ph/0704.2064)
Mantz A., Allen S. W., Ebeling H., Rapetti D. A., 2007, MNRAS, preprint (astro-ph/0709.4294)
Markevitch M. et al., 2003, ApJ, 586, L19
Mason B. S. et al., 2003, ApJ, 591, 540
McCarthy I. G., Bower R. G., Balogh M. L., 2007, MNRAS, 377, 1457
Miknaitis G. et al., 2007, ApJ, 666, 674
Mohr J. J., Evrard A. E., Fabricant D. G., Geller M. J., 1995, ApJ, 447, 8
Mohr J. J., Mathiesen B., Evrard A. E., 1999, ApJ, 517, 627
Molnar S. M., Birkinshaw M., Mushotzky R. F., 2002, ApJ, 570, 1
Montroy T. E. et al., 2006, ApJ, 647, 813
Muanwong O., Thomas P. A., Kay S. T., Pearce F. R., 2002, MNRAS, 336, 527
Nagai D., Vikhlinin A., Kravtsov A. V., 2007a, ApJ, 655, 98
Nagai D., Kravtsov A. V., Vikhlinin A., 2007b, ApJ, 668, 1
Navarro J. F., Frenk C. S., White S. D. M., 1995, ApJ, 275, 720
Navarro J. F., Frenk C. S., White S. D. M., 1997, ApJ, 490, 493
Page L. et al., 2007, ApJS, 170, 335
Pearson T. J. et al., 2003, ApJ, 591, 556
Pen U., 1997, New Astron., 2, 309
Percival W. J. et al., 2007, ApJ, 657, 51
Pfrommer C., Ensslin T. A., Springel V., Jubelgas M., Dolag K., 2007, MNRAS, 378, 385
Piacentini F. et al., 2006, ApJ, 647, 833
Piffaretti R., Jetzer P., Schindler S., 2003, A&A, 398, 41
Pointecouteau E., Arnaud M., Kaastra J., de Plaa J., 2004, A&A, 423, 33
Pratt G. W., Arnaud M., 2002, A&A, 394, 375
Rafferty D. A., McNamara B. R., Nulsen P. E. J., Wise M. W., 2006, ApJ, 652, 216
Rapetti D., Allen S. W., 2007, MNRAS, preprint (astro-ph/0710.0440)
Rapetti D., Allen S. W., Weller J., 2005, MNRAS, 360, 555
Rapetti D., Allen S. W., the Con-X Facility Science Team, 2006, preprint (astro-ph/0608009)
Rapetti D., Allen S. W., Amin M. A., Blandford R. D., 2007, MNRAS, 375, 1510
Rasia E. et al., 2006, MNRAS, 369, 2013
Reynolds C. S., McKernan B., Fabian A. C., Stone J. M., Vernaleo J. C., 2005, MNRAS, 357, 242
Riess A. G. et al., 2004, ApJ, 607, 665
Riess A. G. et al., 2007, ApJ, 659, 98
Roussel H., Sadat R., Blanchard A., 2000, A&A, 361, 429
Ruhl et al., 2004, in Zmuidzinas J., Holland W. S., Withington S., eds, Proc. SPIE, Vol. 5498, Millimeter and Submillimeter Detectors for Astronomy II. SPIE, Bellingham, p. 11
Ruszkowski M., Brüggen M., Begelman M. C., 2004, ApJ, 611, 158
Sanderson A. J. R., Ponman T. J., 2003, MNRAS, 345, 1241
Sasaki S., 1996, PASJ, 48, L119
Schmidt R. W., Allen S. W., 2007, MNRAS, 379, 209
Schmidt R. W., Allen S. W., Fabian A. C., 2004, MNRAS, 352, 1413
Spergel D. N. et al., 2003, ApJS, 148, 175
Spergel D. N. et al., 2007, ApJS, 170, 377
Vikhlinin A., Kravtsov A., Forman W., Jones C., Markevitch M., Murray S. S., van Speybroeck L., 2006, ApJ, 640, 691
White D. A., Fabian A. C., 1995, MNRAS, 273, 72
White D. A., Jones C., Forman W., 1997, MNRAS, 292, 419
White S. D. M., Frenk C. S., 1991, ApJ, 379, 52
White S. D. M., Navarro J. F., Evrard A. E., Frenk C. S., 1993, Nat, 366, 429
Wood-Vasey W. M. et al., 2007, ApJ, 666, 694

This paper has been typeset from a TEX/LATEX file prepared by the author.